Soil Moisture and Hydraulic Parameter Estimation and Remote Sensing for Precision Irrigation

by

Erfan Orouskhani

A thesis submitted in partial fulfillment of the requirements for the degree of

Master of Science

in

Process Control

Department of Chemical and Materials Engineering

University of Alberta

© Erfan Orouskhani, 2022

Abstract

Water scarcities are becoming serious issues worldwide primarily due to population growth, climate change, and increasing pollution. Since a large portion of freshwater is consumed in agricultural activities, with the main consumer being irrigation, increasing the water-use efficiency in irrigation through precision irrigation is a critical step toward reducing the freshwater shortage. Precision irrigation can be achieved by forming a closed-loop irrigation system that closes the irrigation decision loop. To implement the closed-loop irrigation, soil moisture information that is required for feedback control must be provided. In order to obtain the soil moisture information of the entire field, the soil moisture estimation techniques based on the measurements of a small number of sensors are proposed. While soil moisture estimation in agricultural fields is possible, a few main challenges yet exist. Firstly, because of the limited number of available sensors in the agricultural fields, a major challenge is to identify the optimal location of the sensors in the soil so that improved state estimation can be achieved. Additionally, accurate quantification of soil hydraulic parameters, which are crucial for developing an agro-hydrological model and affect its accuracy, is essential for estimating soil moisture. Another challenge associated with soil moisture estimation is converting the remote sensing data into soil moisture that can provide the soil moisture measurements for a large region of the agricultural field. The purpose of this thesis is to find solutions to the aforementioned challenges, resulting in a comprehensive soil moisture estimation method that can be used for closed-loop irrigation.

Firstly, we describe an actual agricultural field in Lethbridge, Canada studied in this

thesis. A three-dimensional agro-hydrological framework is then developed to model the actual field. We specifically use the cylindrical coordinates version of the Richards equation to model a field equipped with a center pivot irrigation system. The heterogeneous distribution of the soil parameters is considered in the Richards model. The modal degree of observability is then applied to the 3D field model to determine the optimal sensor locations in the actual field. The extended Kalman filter is also employed to estimate the soil moisture content of the actual field using the real measurements obtained from the point sensors. The estimation results are then analyzed to investigate the effects of sensor placement on the performance of soil moisture estimation in the actual applications.

To address the second challenge, we propose a systematic estimation approach to simultaneously estimate the soil moisture and soil hydraulic parameters in the 3D agro-hydrological systems with spatially heterogeneous soil parameters. In this part, microwave remote sensors that are mounted on the center pivots are considered to provide the rotating measurements. The sensitivity analysis is employed to determine the most important subset of soil hydraulic parameters for estimation. Another feature of the proposed method is using the Kriging interpolation method for updating the rest parameters that are not estimated. The proposed method is applied to two different simulated three-dimensional fields, and the simulation results of the considered agro-hydrological systems illustrate the applicability and effectiveness of the proposed method on the performance of soil moisture estimation.

Further, the algorithm for surface soil moisture estimation using the thermal and optical remote sensing images is proposed. The machine learning-based Multilayer Perceptron (MLP) model is developed to convert the multispectral images to soil moisture. The developed model is applied to the real agricultural field in Lethbridge and is trained using the experimental data collected in the summer of 2019. The results demonstrate a strong agreement between the measured soil moisture and predicted soil moisture from the MLP model. Throughout this thesis, we demonstrate how the proposed solutions can be used to effectively address the challenges discussed earlier.

Acknowledgments

I would like to thank my supervisor, Dr. Jinfeng Liu, for his guidance and support during my graduate study. Dr. Liu was patient and supportive when I faced obstacles in my research project and in my life.

I would like to thank all my colleagues from Process Systems and Control Engineering group for their support. Special thanks to Bernard Agyeman, Song Bo, Soumya Sahoo, An Zhang, Jianbang Liu, Nirav Raiyani, Sarupa Debnath, Aristarchus Gnanasekar, Benjamin Decardi-Nelson, and Zhiyinan Huang.

I would also like to thank my parents and my brothers, Maysam and Yasin, for their unconditioned support. I want to thank my lovely wife, Kosar Zolfi. Thank you for your love, your support and patience.

I would like to gratefully acknowledge the financial support from Natural Sciences and Engineering Research Council (NSERC) of Canada.

Contents

List of Tables

List of Figures

Chapter 1

Introduction

1.1 Motivation

Water and food scarcities are becoming serious issues worldwide primarily due to population growth, climate change, and increasing pollution. According to United Nations' statistics [6], of the total amount of freshwater, approximately 70 percent is consumed in the agricultural activities, with the main consumer being irrigation. Currently, the average water-use efficiency in irrigation worldwide is about 60 percent as reported in Fischer et al. [7]. That means a significant portion of the water used in irrigation is wasted due to inefficient irrigation strategies. Therefore, it is of vital importance to improve the water-use efficiency in agriculture irrigation, in order to mitigate the freshwater supply crisis. In the current irrigation practice, irrigation in general is determined in an open-loop fashion in which little real-time feedback from the field such as soil moisture is considered. The amount and time of irrigation are typically determined by the farmer based on their experience, which often leads to excessive or insufficient irrigation [8]. One promising solution to address this issue and improve the water-use efficiency is to use a closed-loop irrigation system where a controller uses real-time field conditions to make the best irrigation decisions [9, 10]. Although using the closed-loop irrigation system can lead to optimized irrigation and increased crop yield

and profit, its implementation can be challenging. In the development of such a closed-loop irrigation system, the soil moisture information of the entire field which should be fed back to the controller is required. On the other hand, the agriculture fields usually are of very large scale and installing the sensors in the whole field is impractical. Therefore, one of the main barrier in implementing the closed-loop irrigation system is the lack of field-wide soil moisture measurements. To address this issue, soil moisture estimation techniques that reconstruct full soil moisture information based on the measurements of a small number of sensors have been proposed [11, 1, 12, 13].

However, due to the limited number of available sensors in the agricultural fields, it is an important problem to determine the optimal locations to install the sensors in the soil such that improved soil moisture estimation can be obtained. Furthermore, in soil moisture estimation, an agro-hydrological model is employed to predict the dynamics of the soil moisture content. One of the main important inputs in the agro-hydrological models is the soil hydraulic parameters. These parameters which characterize the properties of the soil, affect the model's accuracy. Thus, the accurate quantification of the soil hydraulic parameters can improve the accuracy of modeling of the agro-hydrological system which leads to more accurate estimates of soil moisture. Therefore, estimating the soil hydraulic parameters is very essential for soil moisture estimation. Estimating the soil hydraulic parameters experimentally in a soil lab is time consuming and expensive especially for large-scale fields with heterogeneous soils. In addition, these parameters may change over time and it would be expensive to take frequent soil samples for lab analysis. An alternative solution is to estimate the soil hydraulic parameters along with the soil moisture at the same time [13]. Further, since it is very expensive to obtain a thorough water distribution of a large-scale field using point sensors, remote sensing techniques typically are employed to obtain soil moisture measurements of the entire field. Converting the remote sensing images to soil moisture is another challenge associated with soil moisture estimation. The above considerations motivate this thesis.

1.2 Literature Review

The literature review consists of three subsections. The first subsection provides a summary of the literature on soil moisture estimation strategies and a detailed discussion of optimal sensor placement. In the second subsection, different approaches to soil hydraulic parameters estimation and the effect of sensitivity analysis on simultaneous state and parameter estimation are discussed. The last subsection discusses remote sensing techniques which are used to provide the soil moisture measurements for a large region of the agricultural field.

1.2.1 Soil Moisture Estimation and Sensor Placement

To address the problem of soil moisture estimation in the agricultural fields, one commonly used type of approach is sequential data assimilation. This approach integrates an agro-hydrological model with small number of soil moisture measurements to estimate the soil moisture of the entire field. In general, in the sequential data assimilation approach, the first step is to use a dynamical system model to describe a real process. In this work, we model the agro-hydrological system using the Richards equation. The Richards equation is a partial differential equation (PDE) that describes the flow of water through unsaturated porous media under the action of gravity and capillarity. However, due to the limited process knowledge and simplifications, the Richards model is unable to predict the soil moisture accurately. Then, in the second step, an algorithm is designed to determine how to correct the predicted soil moisture, based on the field measurements and the Richards model. Moreover, sequential data assimilation has the ability to deal with uncertainties in the measurements and the model.

Popular methods for the sequential assimilation of soil moisture observations include the extended Kalman filter (EKF) [1, 14, 15], the ensemble Kalman filter (EnKF) [16, 17], and the particle filter (PF) [18, 19]. In [14] various assimilation techniques derived from the Kalman Filter were studied. Reichle et al. [15] compared the performance of the EKF

and EnKF methods in the soil moisture estimation of a land surface model, known as the Catchment Model. Based on their study, although the performance of both filters was satisfactory, they had some drawbacks. EKF was computationally expensive due to the Jacobian matrix calculation during linearization, and EnKF required a large number of ensembles for good estimation performance. Walker et al. [20] estimated the soil moisture of the simplified soil moisture model which was the linear version of the Darcy–Buckingham equation, by employing the linear Kalman filter and using real soil moisture measurements. Not considering the root water uptake term, using the simplified soil moisture model instead of Richards' equation which limits its applicability under extreme weather conditions, and investigating the soil moisture estimation for the only one-dimensional system were some shortcomings in their work. De Lannoy et al. [16] used EnKF with real field data to performed bias and regular soil moisture estimation. Although their approach could improve the overall performance of estimation, bias estimation in layers for which no observations were available was impossible. Since the main assumption of Kalman based filters is Gaussian distribution for sensor noise and disturbances, the filter efficiency may drop in the presence of non-Gaussian distribution. To address this problem, some studies used the particle filter in which non-Gaussian distribution in soil data assimilation was considered [19]. Although this approach makes filtering independent on the Gaussian distribution assumption, it may have some problems in updating especially when the realizations are far from the original states [18].

In the above studies, the optimal sensor placement has not been considered. Because of the limited number of available sensors in the agricultural fields, it is an important problem to find the optimal location of the sensors in the soil such that improved state estimation can be obtained. In [21], the problem of optimal sensor placement has been considered. Nahar et al. [21] proposed to use the observability analysis to find the optimal sensor locations. However, the applicability of this method was restricted to one-dimensional systems. In [11], the optimal sensor placement problem has been addressed by employing the modal degree

of observability. It was found that optimally placed sensors can lead to much-improved soil moisture estimation performance. However, it is unclear whether the significantly improved estimation performance can still be observed in the actual applications.

1.2.2 Soil Hydraulic Parameter Estimation and Sensitivity Analysis

The parameters of Richards equation characterize the properties of the soil. As has already been mentioned, the soil hydraulic parameters need to be estimated along with the soil moisture. In this work, we continue using the sequential data assimilation approach to estimate the soil hydraulic parameters. Specifically, we employ this approach to estimate the soil moisture and soil hydraulic parameters simultaneously by augmenting the soil hydraulic parameters as extra states of the dynamic model. In the literature, different studies have been performed to estimate the soil parameters based on the sequential data assimilation approach such as EKF [13, 22], EnKF [23, 24, 25, 26], and PF [27].

In [26], EnKF was used to estimate the soil parameters which were augmented as extra states. In addition, they studied the effective factors on the performance of EnKF. Medina et al. [23] used a dual ensemble Kalman filter (DEnKF) to first estimate the soil moisture by a standard Kalman filter, and then to estimate the soil hydraulic parameters using an unscented Kalman filter. The dual estimation was performed by assimilating near-surface soil moisture observations into the one dimensional Richards equation. In [25], the authors compared three ensemble-based simultaneous state and parameter estimation methods, simultaneous optimization and data assimilation (SODA), augmented EnKF, and dual EnKF to improve the soil moisture estimation accuracy. they demonstrated that the augmented EnKF was the most robust method for general conditions, while SODA was appropriate in addressing the complex situations. Moradkhani et al. [24] employed two EnKFs to separately estimate the soil hydraulic parameters and soil moisture, by assimilating soil moisture measurements into a predictive hydrological model.

One limitation of the above studies is that the observability of the augmented system has not been considered and it is assumed that all parameters are identifiable and estimable. While, because of augmenting the parameters as the extra states, the entire augmented system may not be fully observable which means all parameters may not be estimable. Thus, investigating the observability of the entire system to determine which parameters are identifiable and estimable is an important problem. In [13, 28], this issue has been addressed by performing the sensitivity analysis. Liu et al. [28] showed that the sensitivity analysis plays a key role in simultaneous state and parameter estimation. They demonstrated the sensitivity analysis is able to determine which parameters are identifiable and can be estimated with the states simultaneously. Bo et al. [13] proposed an estimation approach to estimate the soil moisture and soil hydraulic parameters of the one dimensional (1D) agro-hydrological system simultaneously. In this approach, parameter identifiability and sensitivity analysis were used to determine the most important parameters for simultaneous estimation. However, in [13], only 1D agro-hydrological systems with fixed measurements were investigated. Moreover, in all the above studies, homogeneous soil parameters or simple arrangements of different soil types have been considered.

1.2.3 Remote Sensing Techniques For Agriculture

Although in-situ moisture probes (point sensors) are the most reliable soil moisture sensing technique and can provide continuous measurements at various depths of the field, it is very challenging to install point sensors everywhere in the field for obtaining a thorough water distribution [29, 30, 31]. Remote sensing technique is an alternative solution that provides a more practical approach to capturing the spatial variability of soil moisture. The remote sensing images can cover a large region of the agricultural field. The estimation of surface soil moisture using remote sensing methods has been considered in many studies.

Optical remote sensing can be used to determine surface soil moisture. An optical remote sensing-based method examines how soil moisture is related to spectral reflectance.

Angstrom [32] found that the soil moisture increased as reflectance decreased. Weidong et al. [33], studied the relationship between relative reflectance and soil moisture. They demonstrated that at low soil moisture levels, the reflectance was inversely proportional to the soil moisture, whereas it became directly proportional after a certain critical point. In [34], it was indicated that the soil moisture was an exponential function of reflectance. Liu et al. [35] estimated soil moisture by using different methods, including relative reflectance method, derivative method, and difference between absorbance and reflectance method. It has been shown that soil moisture is a nonlinear function of reflectance. In [36], inverted Gaussian function was used to estimate the soil moisture by measuring the reflectance in near-infrared and shortwave infrared wavelengths.

The thermal remote sensing can be also used to estimate the surface soil moisture typically based on the thermal inertia method or temperature index method [37]. For bare soil, land surface temperature represents soil surface temperature, but for cover vegetation, it represents vegetation canopy temperature. In [38], to obtain the soil moisture the normalized difference temperature index method (NDTI) was used. In many studies, optical and thermal infrared remote sensing data have been combined to estimate surface soil moisture. In [39], the temperature-vegetation dryness index (TVDI) was defined as:

$$TDVI = \frac{T_s - T_{s,min}}{T_{s,max} - T_{s,min}}$$

where T_s is the observed land surface temperature at the given pixel, $T_{s,min}$ is the minimum surface temperature, and $T_{s,max}$ is the maximum surface temperature which can be expressed as follows in the triangular method:

$$T_{s,max} = a + bNDVI$$

where NDVI is normalized difference vegetation index, a and b are parameters to fit the data of the dry edge. The TVDI of value 1 represents the dry edge, and value 0 represents the

wet edge.

In Literature, TVDI is widely used to estimate the soil moisture. In [40, 41], a linear function was used to estimate the soil moisture from TVDI. However, in [42, 43], soil moisture was estimated by the nonlinear function of TVDI and fractional vegetation cover. The dry and wet edge theoretically was derived in place of the regression in [43]. In [44], the TVDI method was used to derived the soil moisture and crop yield. The regression results represented the strong correlation between soil moisture and TVDI with the coefficient of determination of $R^2 = 0.61$ to 0.83. In [45], for estimating surface soil moisture, an index called the Temperature Rising Rate Vegetation Index (TRRVDI) was used. This index was derived from the triangular method that utilized the mid-morning land surface temperature rate with the vegetation index. In [46], evaporation fraction (EF) was calculated from the difference between air and surface temperatures vs. the vegetation index triangular plot method. The EF was then used to estimate the soil moisture. Liu et al. [47] estimated the surface soil moisture based on the TVDI method for the heterogeneous regions.

There are some drawbacks in the above studies such as lacking sufficient data for the estimation of model parameters, requiring a large number of pixels to estimate the extreme boundary of a wet and dry region, difficult to validate with the ground soil moisture data due to low resolution, difficult to incorporate uncertainties in the soil moisture models. Esfahani et al. [48] developed artificial neural networks to estimate the soil moisture. They used the high resolution thermal and optical images, different types of vegetation index, and field capacity as inputs to the system. However, their model could not provide enough information for real-time irrigation management due to the low temporal resolution. This issue has been address in [3] by employing long short-term memory recurrent neural networks (LSTM-RNNs) model which is mainly used to handle the sequential data. In [3], the time-varying soil moisture estimation was proposed. In this work, we propose a machine learning based model to estimate surface soil moisture using the high resolution remote sensing images.

1.3 Thesis Outline and Contributions

This thesis is presented in 5 chapters, including this introductory chapter. The thesis is arranged as follows:

Chapter 2 investigates the impact of sensor placement in soil water estimation performance for an actual agricultural field in Lethbridge, Alberta, Canada. First, a description of the actual field and an explanation of the experiments carried out on the field are outlined. The Richards equation is then employed to develop a three-dimensional agro-hydrological model. Heterogeneous distribution of the soil parameters obtained from the interpolation of the soil samples of the studied field is considered in the Richards model. A finite difference (FD) scheme is employed to solve the Richards equation numerically. Subsequently, the modal degree of observability is applied to the 3D field model in order to determine the optimal sensor locations. The Extended Kalman filter (EKF) estimation algorithm is also introduced to estimate the soil moisture content of the studied field. Soil moisture estimation results for different scenarios are obtained and analyzed. The chapter demonstrates the performance of the soil moisture estimation with optimally sensor placement is significantly improved in the actual applications.

In Chapter 3, we propose a systematic estimation approach to estimate the soil moisture and soil hydraulic parameters of the 3D agro-hydrological systems with spatially heterogeneous soil parameters and changing measurements. First, an agro-hydrological system that is equipped with a center pivot irrigation system and microwave soil moisture sensors is introduced. The three dimensional cylindrical coordinates version of the Richards equation is used to model the field equipped with a center pivot irrigation system. This is followed by the construction of the augmented system, which is achieved by augmenting the parameters at the end of the state vector. The sensitivity analysis is then applied to the augmented model to determine the most important parameter set for estimation while the measurements are changing. Next, the EKF estimation algorithm is chosen to simultaneously estimate the soil moisture and the soil hydraulic parameter set determined before. Finally, in order to improve

the performance of estimation, the Kriging interpolation method is employed for updating the unestimated parameters. In the end, soil moisture estimation results are obtained and analyzed to investigate the effectiveness of the proposed method on the performance of soil moisture estimation in the agro-hydrological systems. The chapter demonstrates the proposed approach is able to significantly improve the performance of soil moisture estimation and provide soil moisture estimates with high accuracy and consistency.

In Chapter 4, a supervised estimation of surface soil moisture using a multilayer perceptron (MLP) neural network model is developed. The MLP model is developed to convert the thermal and optical images to soil moisture. A detailed description of how the real data set is created from experimental remote sensing images collected in summer 2019 at Lethbridge is provided. The MLP model is trained using the real data set and the soil moisture estimation results show the effectiveness of the proposed approach.

Chapter 5 provides a conclusion and suggestions for future work.

Chapter 2

Impact of Sensor Placement in Soil Water Estimation: A Real-Case Study

In this chapter, we demonstrate the effectiveness of the optimal sensor placement on the performance of soil moisture estimation in an actual application. We first provide a description of the study area and the experiments carried out on the field in Section 2.1. Then, we develop a mathematical model that is suitable for predicting the dynamics of the soil moisture in the studied field in Section 2.2. Section 2.3 includes the modal degree of observability as a tool to determine the optimal sensor locations and the sensor placement results of the studied field. In Section 2.4, we provide a detailed description of the EKF algorithm adopted for estimating the soil water content of the studied field. A simulation case study is described in Section 2.5 and the effect of the optimal sensor placement on soil moisture estimation is extensively studied based on the simulations. In Section 2.6, real measurements provided by probe sensors are considered. Two different scenarios are constructed to investigate the impact of sensor placement in soil water estimation for the actual application. This is followed by concluding remarks in Section 2.7.

2.1 Description of the Studied Field

This section describes the actual agricultural field studied in this thesis and discusses the experiment conducted on the field in summer 2019. Two main steps of the experiment include: 1) Soil sample collection for texture analysis; 2) Soil moisture data collection for ground truth. First, we describe the details of the study area. The soil sample collection procedure is then discussed and finally, we discuss the soil moisture data collection procedure.

2.1.1 Study Area

(a) The center pivot irrigation system of the field.

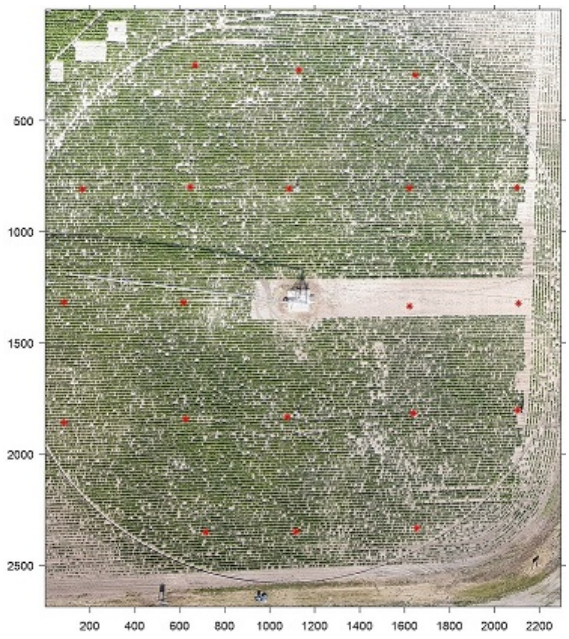

(b) Location of the sensors in the studied field.

Figure 2.1: Illustration of the studied field in Lethbridge.

The agricultural field studied in this work is located in Lethbridge, Alberta, Canada (Lon: -112.7385 : -112.7365, Lat: 49.6896 : 49.6908). The field is a circular one with a radius of about 50 meters. The depth of the field is 75 cm in the simulations of this work. One weather station is located near the agricultural studied field managed by Lethbridge Demo Farm Irrigation Management Climate Information Network (IMCIN). The weather station's data including the precipitation, wind speed, and air temperature can be obtained from the

Alberta Climate Information Service (ACIS) website (https://agriculture.alberta.ca/acis/). The soil texture consists of three types of soil: clay, silt, and sand. Each area of the field has a different percentage of the soil types that makes the soil profile heterogeneous. Thus, the soil profile of the field has different properties at various zones. For example, on the left side of the field where the percentage of the clay in the soil is higher than other areas of the field, the water infiltration to the root zone is slower compared to other areas. In the studied field, a centre pivot is used as the irrigation implementing system as shown in Figure 2.1(a). In irrigation time, the center pivot rotates at a speed of 0.011 m/s, which means, the central pivot usually takes 8 hours to irrigate the whole field.

2.1.2 Soil Texture and Moisture Data Collection

The soil parameters of the field model depend upon the properties of soil existing in the field. In this thesis, we obtain the soil parameters of the model from the soil texture experiment. The soil profiles at 60 points of the studied field (20 points from surface to depth 25 cm, 20 points at 25 cm to 50 cm, and 20 points at 50 cm to 75 cm) were sampled using augers (Figure 2.2(a)). After collecting the soil sample, the soil properties of the sampling points including the wilting point, the electrical conductivity of the water, and the percentage of the clay, silt, and sand existing in the soil samples were estimated in the soil lab. The soil profile data will be used in Section 2.2.2 to interpolate the soil parameters of the entire field. The interpolated soil parameters will be used as the field model parameters.

(a) Soil sample collection.

(b) Data logger, Multiplexer, Solar panel and Sensors.

Figure 2.2: Sensing instruments used in the experiment.

Moreover, 42 sensors [49] were installed in the field at different depths (14 sensors at the depth of 25 cm, 14 sensors at the depth of 50 cm, and 14 sensors at the depth of 75 cm, below the surface) to measure the soil water tension of these locations. The measurements were collected every 60 minutes from June 19 to August 13, 2019. Figure 2.1(b) shows the location of the sensors in the studied field. During the experiment, a data logger was used to collect the data from the sensor. Since the data logger did not have enough ports to connect all forty-two sensors, a multiplexer was used to connect the sensors to a single data logger. In the whole field, we employed two data loggers and two multiplexers for data collection. Two solar panels were also installed to charge the data loggers. The data logger, multiplexer and solar panel are shown in Figure 2.2(b). Some irregular features in the collected data set were observed, which increase the model plant mismatch and cause the overall soil moisture estimation more challenging. The collected data will be used in Section 2.6 to estimate the soil moisture of the entire field through a state estimator.

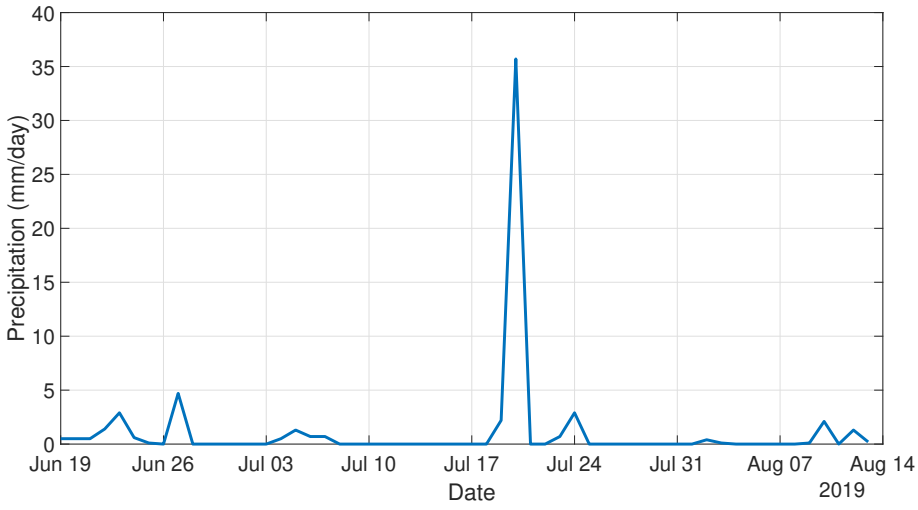

Figure 2.3: Daily precipitation data of the studied field during the period under investigation.

The precipitation data of the studied field obtained from ACIS is illustrated in Figure 2.3 on a daily basis for the period under investigation. According to statistics, there was a substantial amount of rain on July 20.

2.2 Modeling of the Water Dynamics of the Studied Field

2.2.1 Agro-hydrological System Description

An agro-hydrological system characterizes the hydrological cycle between the soil, the water, the atmosphere, and the crop. In this work, the three dimensional agro-hydrological model is considered in which the water inflows to the system are rainfall and irrigation, and the system outflows are evaporation, transpiration, run-off, and drainage. Figure 2.4 provides an illustration of an agro-hydrological system, from [1]. Depending on the water condition in the soil, rain or irrigation water may enter the soil at its surface. When the soil is unsaturated, water infiltrates into the soil and this continues until the soil becomes saturated. Under saturated conditions, the infiltration tends to cease and ponding starts to occur. After a

certain ponding height, the water level breaks and run-off sets in. A portion of the rain or irrigated water may not reach the soil surface and be intercepted by the crop canopy. The roots of crops act as water sinks that extract water from the soil.

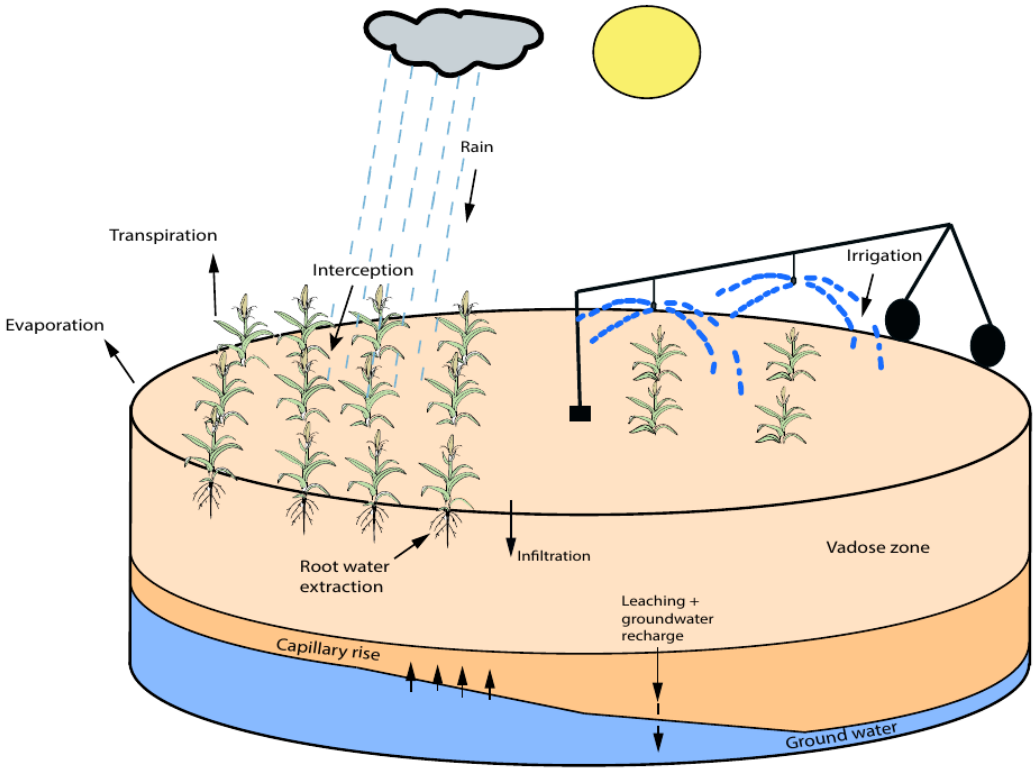

Figure 2.4: An agro-hydrological system [1].

In this work, we focus on soil that is above the water table, known as the vadose zone. Within the vadose zone, the water movement is mainly driven by capillary and gravitational forces and the water dynamics can be modeled using Richards equation [50] as follows:

$$\frac{\partial \theta}{\partial t} = C(h)\frac{\partial h}{\partial t} = \nabla \cdot (K(h)\nabla(h+z)) - S \tag{2.1}$$

where h (m) is the pressure head, θ (m^3m^{-3}) is the volumetric water content, t (s) is time, z (m) is the spatial coordinate, $K(h)$ (ms^{-1}) is the unsaturated hydraulic water conductivity, $C(h)$ (m^{-1}) is the capillary capacity, and S $(m^3m^{-3}s^{-1})$ denotes the sink term, representing the root water extraction rate.

In Equation (2.1), the soil hydraulic functions $\theta(h)$, $K(h)$, and $C(h)$ can be obtained by the Mualem-van Genucthen model [51]:

$$\theta(h) = \theta_r + (\theta_s - \theta_r)\left[\frac{1}{1+(-\alpha h)^n}\right]^{1-\frac{1}{n}} \tag{2.2}$$

$$K(h) = K_s\left[(1+(-\alpha h)^n)^{-\left(\frac{n-1}{n}\right)}\right]^{\frac{1}{2}} \times \left[1-\left[1-\left[(1+(-\alpha h)^n)^{-\left(\frac{n-1}{n}\right)}\right]^{\frac{n}{n-1}}\right]^{\frac{n-1}{n}}\right]^2 \tag{2.3}$$

$$C(h) = (\theta_s - \theta_r)\ \alpha n\ (1-\frac{1}{n})\ (-\alpha h)^{n-1}\left[1+(-\alpha h)^n\right]^{-\left(2-\frac{1}{n}\right)} \tag{2.4}$$

where θ_s (m^3m^{-3}), θ_r (m^3m^{-3}), K_s (ms^{-1}) are the saturated volumetric moisture content, residual moisture content and saturated hydraulic conductivity, respectively. n and α are curve-fitting soil hyrdraulic properties. The parameters $\theta_s, \theta_r, K_s, \alpha$, and n form a set of soil hydraulic parameters that determine the soil properties of the field.

2.2.2 Interpolation of Soil Parameters

Saturated hydraulic conductivity K_s $(\frac{m}{s})$, saturated soil moisture θ_s $(\frac{m^3}{m^3})$, residual soil moisture θ_r $(\frac{m^3}{m^3})$, and curve-fitting soil hydraulic properties α $(\frac{1}{m})$ and n are the soil parameters of the model. Each type of the soil has its own set of soil parameters. Due to the heterogeneity of the soil in the studied field, the soil parameters are different at different points of the field. In fact, each point in the field which corresponds to a node in the discretized model has its own set of soil parameters. These soil parameters are unknown and need to be obtained. In this work, we use the Kriging interpolation method to estimate the soil parameters of the entire field. The Kriging interpolation method is an advanced geostatistical method that produces an estimated surface from a small number of scattered measurements. The Kriging

formula is formed as a weighted sum of the data [52]:

$$\hat{Z}(s_o) = \sum_{i=1}^{N} \lambda_i Z(s_i) \tag{2.5}$$

where $\hat{Z}(s_o)$ is the Kriging predicted value at the prediction location, $Z(s_i)$ denotes the measured value at the measured i^{th} location, N is the total number of measurements, and λ_i is a weight between the measured value at i^{th} location and the predicted value at the prediction location.

Both the distance between the measured locations and the prediction location, and the overall spatial positioning of the measured locations may affect the weights. The weights $(\lambda_i, i = 1, 2, ...N)$ can be obtained from the following matrix equation [53]:

$$\begin{bmatrix} a_{11} & a_{12} & \dots & a_{1n} \\ a_{21} & a_{22} & \dots & a_{2n} \\ \vdots & \ddots & \vdots & \\ a_{n1} & a_{n2} & \dots & a_{nn} \end{bmatrix} \cdot \begin{bmatrix} \lambda_1 \\ \lambda_2 \\ \vdots \\ \lambda_n \end{bmatrix} = \begin{bmatrix} b_1 \\ b_2 \\ \vdots \\ b_n \end{bmatrix} \tag{2.6}$$

where a_{ij} is the semivariance value between the measured points i and j, λ_i is the weight between the measured point i and the prediction location, and b_i is the semivariance value between the measured point i and the prediction location. All the semivariance values are obtained from the semivariogram graph in which the x-axis is the distance between the points and the y-axis is the semivariance. The procedure to obtain the semivariogram graph consists of the following steps:

(1) Measure some specific points of the field. Each measurement includes two compartments; the coordinate of the point and the measured value of the point.

(2) Calculate the distances of each pair for all the measured points.

(3) Perform variogram calculations based on the same distances obtained in step 2, using

the following formula; where h_{ij} is the distance between the measured i^{th} and j^{th} points, $Z(s_i)$ and $Z(s_j)$ are the measured values at the i^{th} and j^{th} locations, respectively, and $\mu(h)$ is the semivariance for each same distance [53].

$$\mu(h) = \frac{\sum_{h_{ij}=h}[Z(s_i) - Z(s_j)]^2}{2N} \tag{2.7}$$

(4) Fit a model to the points whose x element is the distances calculated in step 2 and y element is the semivariances obtained in step 3. Four main functions (spherical, exponential, gaussian, and linear) can be used to model the points. In this work, we use the spherical function, Equation (2.8), to fit the points. In Equation (2.8) μ_0 (nugget) is the value of the semvariance when the distance is zero, μ_{ss} (sill) is the value of the semivariance when it remains constant, and α (range) is a certain distance where the semivariance values will stop changing.

$$\mu(h) = \begin{cases} \mu_0 + \mu_{ss}[\frac{3h}{2\alpha} - \frac{1}{2}(\frac{h}{\alpha})^3] & h \leq \alpha \\ \mu_{ss} & \alpha \leq h \end{cases} \tag{2.8}$$

(5) Find all the semivariance values are required in the Equation (2.6), using the semivariogram graph obtained in step 4.

The following paragraph explains how the Kriging interpolation method that was described earlier was used to calculate the heterogeneous distribution of soil parameters in the studied field based on the soil samples taken from the study area. We first used the 60 soil samples of the studied field and determined the soil texture type of the sampled points by measuring the percentage of the clay, silt, and sand soils existing in the samples. Next, we obtained the set of soil parameters for these sampling points based on the composition of the soil types [54]. Subsequently, we used the soil parameters of these 60 sampled points as the measurements in the Kriging interpolation method to interpolate the soil parameters of the

entire field. Figure 2.5 shows the interpolated soil parameters of the surface of the studied field. The results show that the soil parameters of the field are heterogeneous.

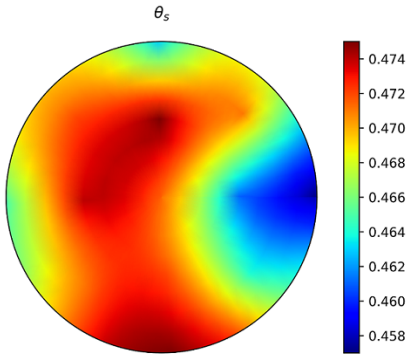

(a) Saturated volumetric moisture content (θ_s (m^3m^{-3}))

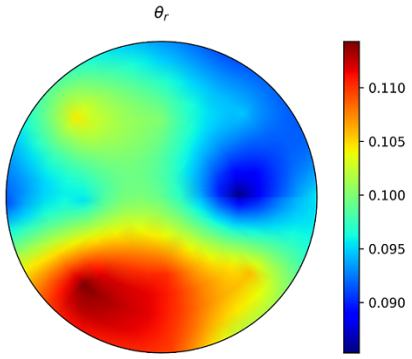

(b) Residual moisture content (θ_r (m^3m^{-3}))

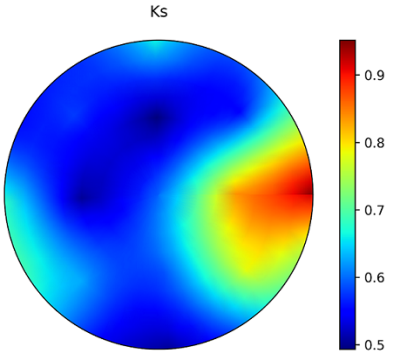

(c) Saturated hydraulic conductivity (K_s ($cmhr^{-1}$)

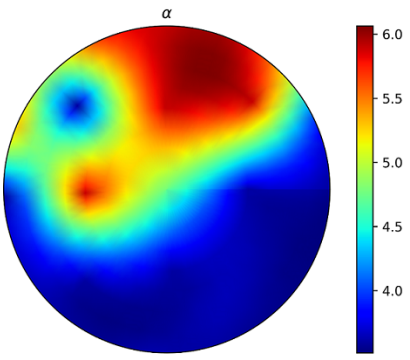

(d) Curve fitting parameter (α (m^{-1}))

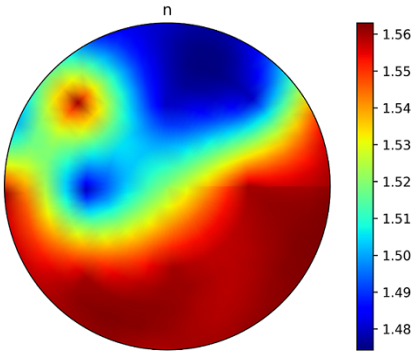

(e) Curve fitting parameter (n)

Figure 2.5: Heterogeneous distribution of soil parameters on the surface of the studied field obtained from the Kriging interpolation.

2.2.3 Polar Form of Richards Equation

In [1], it was demonstrated that the cylindrical coordinate version of the Richards equation is very suitable for the modeling of an agricultural field equipped with a center pivot irrigation system due to its ability to account for the circular movement of the center pivot. Therefore, since the center pivot is used as the irrigation implementing system in the studied field, we will use the cylindrical coordinate of the Richards equation in this work. Cylindrical coordinate representation of the Richards equation is expressed as follows [1]:

$$C(h)\frac{\partial h}{\partial t} = \frac{1}{r}\frac{\partial}{\partial r}\left[rK(h)\frac{\partial h}{\partial r}\right] + \frac{1}{r}\frac{\partial}{\partial \theta}\left[\frac{K(h)}{r}\frac{\partial h}{\partial \theta}\right] + \frac{\partial}{\partial z}\left[K(h)\left(\frac{\partial h}{\partial z} + 1\right)\right] - S \tag{2.9}$$

where r (m) represents the radial direction which denotes the radius of the field, θ represents the azimuthal direction which denotes the angle of rotation of the center pivot, and z (m) is the axial direction which represents the depth of soil under consideration. Equation (2.9) is a nonlinear parabolic-elliptical partial differential equation (PDE) with respect to the temporal (t) and the spatial variables ($r,\ \theta,\ z$).

2.2.4 Model Discretization

Obtaining an analytical solution to Equation (2.9) is difficult due to its nonlinearity, thus numerical solutions are needed to solve this equation. In [1], the method of lines (MOL) approach was used to solve the Richards equation numerically and discretize the Equation (2.9) with respect to its spatial variables. The same numerical model development and discretization scheme is used in this work. In the following, we summarize the model development.

Firstly the two point central finite difference scheme is employed to approximate the derivatives of Equation (2.9) with respect to the spatial variables ($r,\ \theta,\ z$). This converts the PDE into a set of ordinary differential equations (ODEs) in terms of the temporal variable (t), which can then be solved using well established numerical methods for ODEs. The detailed approximation procedure in the r, θ, and z directions is described in [1]. Once

the discretization in the radial (r), azimuthal (θ), and axial (z) directions are obtained, the resulting ODE, in terms of the temporal variable, can be obtained by substituting discretization equations into the Equation (2.9) as follows:

$$\frac{dh}{dt} = \frac{1}{C_{e_r,e_\theta,k}(h)}\Bigg[\Bigg(\frac{1}{r_{e_r,e_\theta,k}\Delta r_i}\Bigg[r_{e_r+\frac{1}{2},e_\theta,k}K_{e_r+\frac{1}{2},e_\theta,k}(h)\Bigg(\frac{h_{e_r+1,e_\theta,k}-h_{e_r,e_\theta,k}}{\Delta r_E}\Bigg)- r_{e_r-\frac{1}{2},e_\theta,k}K_{e_r-\frac{1}{2},e_\theta,k}(h)\Bigg(\frac{h_{e_r,e_\theta,k}-h_{e_r-1,e_\theta,k}}{\Delta r_W}\Bigg)\Bigg]\Bigg)+ \Bigg(\frac{1}{r_{e_r,e_\theta,k}\Delta\theta_j}\Bigg[\frac{K_{e_r,e_\theta+\frac{1}{2},k}(h)}{r_{e_r,e_\theta+\frac{1}{2},k}}\Bigg(\frac{h_{e_r,e_\theta+1,k}-h_{e_r,e_\theta,k}}{\Delta\theta_T}\Bigg)- \frac{K_{e_r,e_\theta-\frac{1}{2},k}(h)}{r_{e_r,e_\theta-\frac{1}{2},k}}\Bigg(\frac{h_{e_r,e_\theta,k}-h_{e_r,e_\theta-1,k}}{\Delta\theta_D}\Bigg)\Bigg]\Bigg)+ \Bigg(\frac{1}{\Delta z_k}\Bigg[K_{e_r,e_\theta,k+\frac{1}{2}}(h)\Bigg(\frac{h_{e_r,e_\theta,k+1}-h_{e_r,e_\theta,k}}{\Delta z_N}+1\Bigg) - K_{e_r,e_\theta,k-\frac{1}{2}}(h)\Bigg(\frac{h_{e_r,e_\theta,k}-h_{e_r,e_\theta,k-1}}{\Delta z_S}+1\Bigg)\Bigg]\Bigg) - S(h,z)\Bigg] \quad (2.10)$$

To solve the resulting ODE, the left side of Equation (2.10) needs to be approximated. In this work, we use the Backward Differentiation Formulas (BDFs) methods to approximate the time derivative in Equation (2.10). To implement the BDFs methods, the 'cvodes' integrator in CasAdi (version 3.5.1) is used.

Specifically, in this chapter, we discretize the field into 6, 40 and 22 nodes in the radial, azimuthal and axial directions, respectively. The head pressure of the soil at these discretized nodes are the states of the system. Furthermore, Equation (2.9) is solved numerically for the following initial and boundary equations which apply to fields equipped with a center pivot irrigation system:

$$h(r,\ \theta,\ z,\ t=0) = h_{initial} \tag{2.11}$$

$$\left.\frac{\partial h\,(r,\theta,z,t)}{\partial r}\right|_{(r=0,\ \theta,\ z)} = 0 \tag{2.12}$$

$$\left.\frac{\partial h\,(r,\theta,z,t)}{\partial r}\right|_{(r=H_r,\ \theta,\ z)} = 0 \tag{2.13}$$

$$\left.\frac{\partial h\,(r,\theta,z,t)}{\partial \theta}\right|_{(r=0,\ \theta,\ z)} = 0 \tag{2.14}$$

$$\left.\frac{\partial h\,(r,\theta,z,t)}{\partial z}\right|_{(r,\ \theta,\ z=0)} = 0 \tag{2.15}$$

$$\left.\frac{\partial h\,(r,\theta,z,t)}{\partial z}\right|_{(r,\ \theta,\ z=H_z)} = -1 - \frac{u_{\text{irr}}}{K(h)} \tag{2.16}$$

$$h(r,\ \theta=0,\ z,\ t) = h(r,\ \theta=2\pi,\ z,\ t) \tag{2.17}$$

where H_r in Equation (2.13) is the total radius of the field, H_z in Equation (2.16) is the length of the soil column and u_{irr} (m/s) represents the irrigation rate which is considered as the input in this work. The zero gradient boundary condition is imposed at $r = 0$ and $r = H_r$ as shown in Equations (2.12) and (2.13). After one rotation of the center pivot, the starting point coincides with the ending point and this is represented by Equation (2.17). Equation (2.15) represents the free drainage boundary condition that is applied at the bottom of the field ($z = 0$). The Nuemann boundary condition, shown by Equation (2.16), is used at the top of the field ($z = H_z$) to incorporate the irrigation rate into the Richards equation.

2.2.5 State-space Representation of the Field Model

By combining $(N_r\ +1) \times (N_\theta\ +1) \times (N_z\ +1)$ of Equation (2.10) for all the spatial nodes and boundary conditions, Equations (2.11) - (2.17), a compact form of the field model can be obtained. Thus, the state-space representation of the field model is expressed as:

$$\dot{x}(t) = F(x(t), u(t)) + \omega(t) \tag{2.18}$$

where $x(t) \in \mathbb{R}^{N_x}$ represents the state vector containing $N_x = 5,280$ pressure head values for the corresponding spatial nodes. $u(t) \in \mathbb{R}^{N_u}$ and $\omega(t) \in \mathbb{R}^{N_x}$ represent the input vector and the model disturbances respectively. Specifically, in this work, the sensors directly measure the states of the system and the output vector $y(k)$ is the head pressure (h) at the measured nodes of the field. Thus, the output equation simply represents a matrix (C) indicating which states are measured by the sensors:

$$y(t) = Cx(t) + v(t) \tag{2.19}$$

where $y(t) \in \mathbb{R}^{N_y}$ and $v(t) \in \mathbb{R}^{N_y}$ respectively denote the measurement vector and the measurement noise. The matrix C is determined by the sensor placement algorithm.

2.3 Optimal Sensor Placement

In order to determine the best locations to install the sensors in the agricultural fields, Sahoo et al. [11] proposed to use the modal degree of observability. They demonstrated that the degree of observability tells us how strongly or weakly observable a system is and it can be used as a measure of the optimality of sensor placement. In this work, we use the algorithm presented in [11]. In the following, we summarize the algorithm.

Modal degree of observability inspired by the PBH test analyzes the ability of a sensor node to estimate other nodes of the system. In the PBH test, if the entry of the right eigenvector v_{ij} is zero, then the j^{th} node is not observable by measuring the i^{th} node. Based on the extension of this test, Gu et al. [55] proposed that the node j is weakly observable from the sensor node i, if the entry of v_{ij} is small. Thus, this approach is able to find the

nodes that are difficult to estimate from a sensor node and subsequently helps us to find the optimal sensor locations. For a node i at a specific time k, the normalized measure of the modal degree of observability can be calculated as [56]:

$$O_i^{(k)} = \sum_{j=1}^{n} (1 - \lambda_j^2(A_d^{(k)}))v_{ij}^2 \tag{2.20}$$

where $A_d^{(k)}$ is the discretized model Jacobian matrix at time k that can be obtained from $A_d^{(k)} = e^{A(k)T}$ when T is the sampling time, and $\lambda_j (j = 1, \ldots, n)$ are the eigenvalues of matrix $A_d^{(k)}$. Based on the definition in [11], the degree of observability of the system is the highest when the sensors are located at nodes with the highest degree of observability. Thus, the determination of the optimal sensor placement which is based on the maximization of the degree of observability, consists of three steps:

1. At a time instant k, calculate the normalized measure of the modal degree of observability $O_i^{(k)}$ for all the system nodes $i, i = 1, \ldots, n$, where n is the total number of the states.

2. Compute the final modal degree of observability (O_i) for each node as the average value of the modal degree of observability over all the time instants.

3. Order the measures $O_i, i = 1, \ldots, n$, according to their values. The optimal locations to place the sensors are the nodes with the highest O_i values.

Since in this method it is not required to consider all the combinations of the sensors and in order to determine the optimal sensor placement we only have to calculate the O_i values for all the states, order them, and find the biggest O_i value, this approach is computationally very efficient especially for large-scale systems such as the three-dimensional agro-hydrological system. In the following, we describe how the above sensor placement algorithm can be applied to the system considered in this work.

Firstly, the system in Equation (2.18) is simulated numerically and the state trajectory

$(x(t))$ of the system is obtained during the simulation. Then, a symbolic approach using CasAdi [57] is employed to calculate the Jacobian matrix (A) which is required in implementation of the optimal sensor placement algorithm. In calculation of Jacobian matrix, the state trajectory obtained from the previous step is required at each operating point (k). Next, we calculate the discretized model Jacobian matrix from $A_d(k) = e^{A(k)T}$ and use it in Equation (2.20) to obtain the degree of observability for all nodes of the system at a specific operating point. Eventually, the final modal degree of observability for each node is the average of the modal degree of observability values obtained at the operating points.

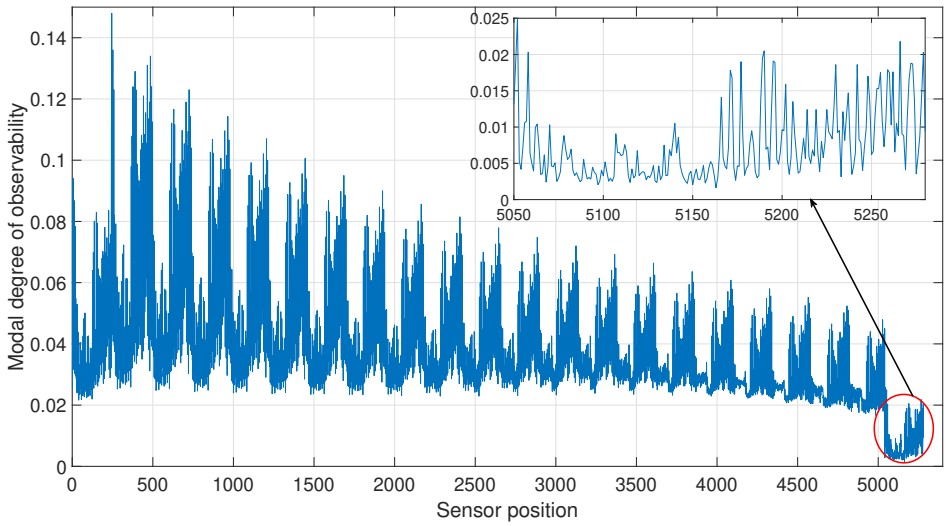

Figure 2.6: Average modal degree of observability for different nodes of the system.

Figure 2.6 represents the modal degree of observability for different nodes of the system considered in this work. From Figure 2.6, it can be seen that nodes between 240 and 480, located at 65 cm below the surface layer, have relatively higher values of the modal degree of observability around 0.0574, while placing sensors on the surface corresponding to nodes 5040 to 5280 gives the lowest modal degree of observability about 0.0075. Furthermore, the location of the optimal sensor placement is node 244 which has the highest degree of observability value, 0.148.

2.4 Soil Moisture Estimator Design

Once the system observability is checked and the optimal sensor placement is found, state estimation can be performed. The nonlinear state estimators should be used to estimate the states of the agro-hydrological model due to its nonlinearity. In this work, we choose the discrete-time extended Kalman filter (EKF) to estimate the states. The EKF algorithm consists of two steps, the prediction step, and the update step. In the prediction step, the state x and its covariance matrix P are predicted using the model of the system. In the update step, the prediction values x and P are updated using the actual measurements. The detail steps are described as follows:

Initialisation

1. The continuous-time system, Equations (2.18) and (2.19), is discretized to obtain its discrete-time equivalent. The discrete-time version can be expressed as:

$$\begin{aligned} x_{k+1} &= f(x_k, u_k) + \omega_k \\ y_k &= Cx_k + v_k \end{aligned}$$

   and the filter is initialized with $\hat{x}_0$ and $P_{0|0}$.

Prediction

1. The new state of the system is predicted at time t_{k+1}, using the previous state estimate $\hat{x}_{k|k}$ and its covariance matrix $P_{k|k}$, and the new input u_k to the system:

$$\hat{x}_{k+1|k} = f(\hat{x}_{k|k}, u_k)$$

2. The state covariance matrix is obtained by

$$P_{k+1|k} = A_k P_{k|k} A_k^T + Q$$

where $A_k = \frac{\partial f}{\partial x}|_{\hat{x}_{k|k},\ u_k}$ and Q is the covariance matrix of the process disturbance ω. In this work, we use a symbolic approach using CasAdi to calculate the Jacobian matrix (A).

Filtering

1. We use the observation y_{k+1} at time t_{k+1} to update the state and its covariance matrix. The observation vector includes the states are measured by the sensors. The location of the sensors is determined by the optimal sensor placement algorithm. Kalman gain matrix, G_{k+1} can be calculated as

$$G_{k+1} = P_{k+1|k}C^T[CP_{k+1|k}C^T + R]^{-1}$$

where R is the covariance matrix of the measurement noise v.

2. Once the updated Kalman gain is obtained, the state is updated:

$$\hat{x}_{k+1|k+1} = \hat{x}_{k+1|k} + G_{k+1}[y_{k+1} - C\hat{x}_{k+1|k}]$$

3. The state covariance matrix is updated as follows

$$P_{k+1|k+1} = [I - G_{k+1}C]P_{k+1|k}$$

In this work, we rely on extensive simulations to determine the appropriate tuning EKF parameters (matrices P, Q and R). We examine the estimated state trajectories and estimation error for different tuning parameters and choose tuning matrices that improve significantly the estimation performance and result in a smaller estimation error. In the tuning matrix P, it is notable to mention that since our knowledge of the initial estimate of the state $\hat{x}_0$ is limited in the real case study, a high initial covariance matrix ($P_{0|0} = \infty I$) must be chosen.

2.5 Initial Simulation Study

In this section, we evaluate the modal degree of observability results for large-scale three-dimensional agro-hydrological systems using state estimation with simulated data. The three-dimensional agro-hydrological system obtained in Section 2.2, is used to simulate the model and obtain the head pressure of the actual system and is further used in the prediction step of the estimator. In the agro-hydrological model, the interpolated soil parameters obtained in Section 2.2.2 are used as the parameters of the model. Thus, heterogeneous soil parameters are considered in the simulations. In addition to the soil parameters, the initial condition of the head pressure (x_0) is also non-uniform and each state of the system has a different initial condition. In this study case, the initial condition of the states in the actual system is a random variable between -0.95 m and -0.8 m. The irrigation amount is a constant rate of 3.6 mm/day which is applied to the farm in the first 8 hours of each day, between 0:00 AM to 8:00 AM.

As we discussed in Section 2.2.4, the studied field is discretized into 5280 nodes (states) with 6 nodes in the radial direction, 40 nodes in the azimuthal direction, and 22 nodes in the axial direction. The first reason to choose these number of nodes for discretizing the field is to produce the nodes in the model that are matched with the actual measurement locations in the actual field. In fact, the number of nodes in the radial and azimuthal directions and hence Δr and $\Delta\theta$ were selected based on the location of the forty-two sensors in the studied field. In addition, it was observed that further mesh refinement in any of the three directions did not result in a significant change in the state trajectories. Thus, it is considered that an accurate numerical approximation of Equation (2.9) can be achieved with 5,280 states. Figure 2.7 shows a schematic diagram of the studied field with its mesh structure, from [1]. Additionally, based on the fact that the center pivot of the studied field takes about 8 hours to fully traverse the whole field and we divided the whole field in the azimuthal direction into 40 compartments, the appropriate time step size for the temporal discretization is about 12 minutes.

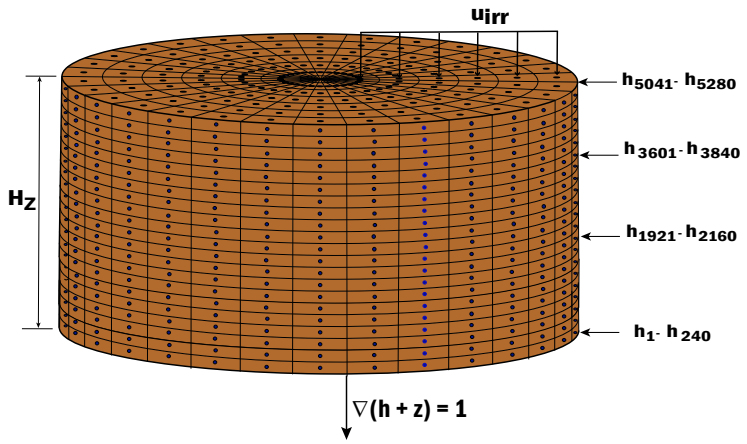

Figure 2.7: A schematic diagram of the studied field [1].

In EKF design, 20% mismatch in the initial condition of each state is considered. Twelve head pressure measurements at fixed locations in the field are used to correct the prediction in the update step of the EKF at each sampling time. Process noise and measurement noise are considered in the simulations and they have zero mean and standard deviations of 1×10^{-6} and 6×10^{-2}, respectively. In the following simulations, we will compare the trajectories of the actual states and EKF estimated states for some selected nodes in order to observe the ability of the EKF for tracking the actual states and investigate the effect of sensor placement on the performance of state estimation. Additionally, the root mean square error (RMSE) at a time instant and the average RMSE will be calculated to assess the estimation performance:

$$RMSE_x(k) = \sqrt{\frac{\sum_{i=1}^{n_x}(\hat{x}_i(k) - x_i(k))^2}{n_x}} \tag{2.21}$$

$$RMSE_x = \frac{\sum_{k=0}^{N_{sim}-1} RMSE_x(k)}{N_{sim}} \tag{2.22}$$

where $\text{RMSE}_x(k)$ with $k = 0, \cdots, Nsim - 1$ shows the evolution of the RMSE value over time and RMSE_x shows the average value. In order to fairly compare the performance of state estimation between different scenarios we use the normalized RMSE ($NRMES = \frac{RMSE}{\bar{y}}$) which facilitates the comparison between datasets or models with different scales.

To verify the effectiveness of the proposed method, two different cases are considered. In the first case, the sensors are placed at 12 nodes with a higher degree of observability, around 1.8056, and the second case is where 12 sensors correspond to nodes with a lower degree of observability, about 0.2937. Figure 2.8 represents the trajectories of the actual states and estimated states for cases 1 and 2 at some testing nodes.

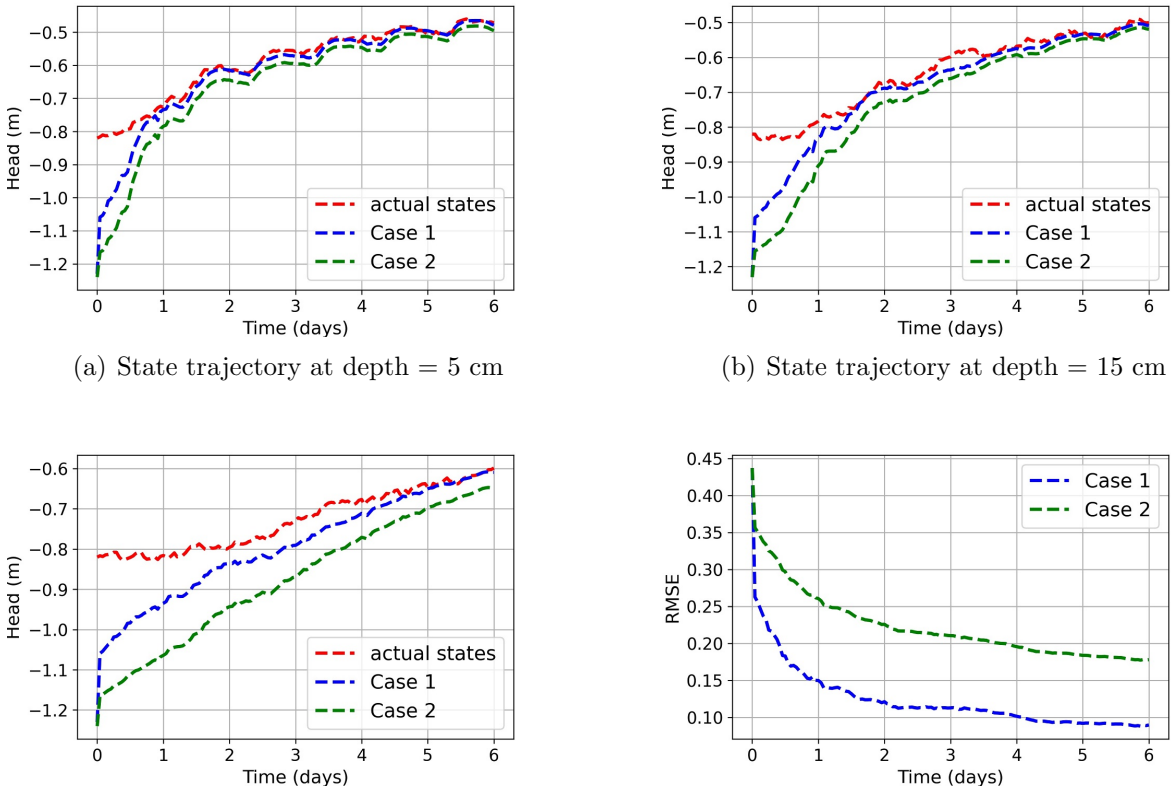

(a) State trajectory at depth = 5 cm

(b) State trajectory at depth = 15 cm

(c) State trajectory at depth = 30 cm

(d) Total estimation error trajectory

Figure 2.8: Estimation results using simulated data. (a)-(c) Trajectories of the actual states (red lines), estimated states in case 1 (blue lines), and estimated states in case 2 (green lines) at depth of (a) 5 cm, (b) 15 cm, and (c) 30 cm, below the surface. (d) Evolution of the RMSE of the original state vector during the simulation time in case 1 (blue lines) and case 2 (green lines).

From Figure 2.8, firstly it can be seen that the EKF (blue, green dash-dot) estimates are able to track the actual process states (red dash-dot) very well. Secondly, it can be observed that the estimates by placing the sensors with higher degree of observability converge faster to the actual states. Figure 2.8(d) compares the total estimation error between case 1 and

case 2 and it demonstrates that the root mean square error (RMSE) in case 1 is smaller than case 2 over the simulations. Also, the average NRMSE over 6 days simulations in case 1 is 15.95% while in case 2 is 28.70%. Thus, optimally placed sensors can improve the soil moisture estimation performance for the three-dimensional agro-hydrological system with heterogeneous soil parameters and initial conditions when the simulated data is used. As a further analysis, we construct the actual and estimated soil water content maps to examine the performance of state estimation for a large number of states. We also construct the absolute error maps by computing the absolute error (e_k) between the actual soil water content and the estimated soil water content.

$$e_k = x_k - \hat{x}_k \tag{2.23}$$

Figures 2.9-2.12 represent the soil water content maps constructed at selected times during the simulation period for the surface of the field in case 1 where the optimal sensor placement is considered. From the Figures, it is observable that the agreement between the estimated maps and the actual maps is significantly strengthened as the simulation time proceeds. Specifically, based on the Figures 2.9 and 2.12, the range of the absolute error on the second day is between 0.005 and 0.02, while on the fifth day it decreases to the range of 0.001 and 0.005.

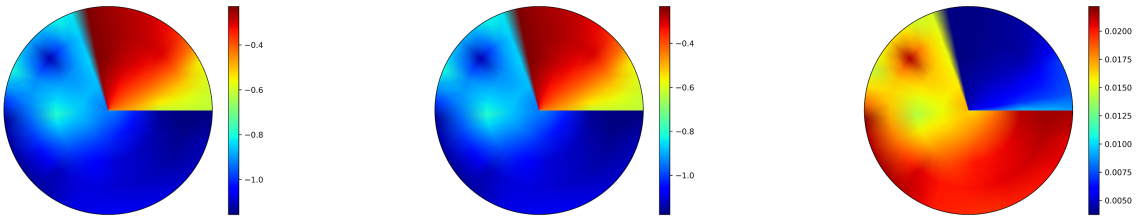

(a) Actual map (b) Estimated map (c) Absolute error map

Figure 2.9: Surface soil water content maps at 02:24 HRS on Day 2 in case 1.

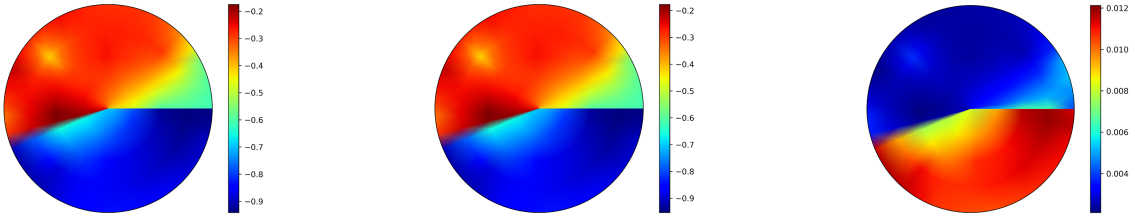

(a) Actual map (b) Estimated map (c) Absolute error map

Figure 2.10: Surface soil water content maps at 04:24 HRS on Day 3 in case 1.

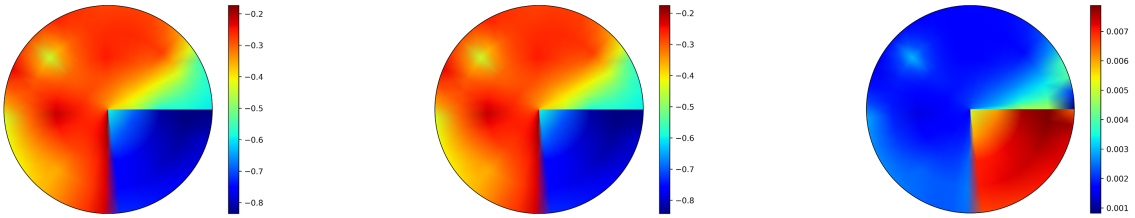

(a) Actual map (b) Estimated map (c) Absolute error map

Figure 2.11: Surface soil water content maps at 06:00 HRS on Day 4 in case 1.

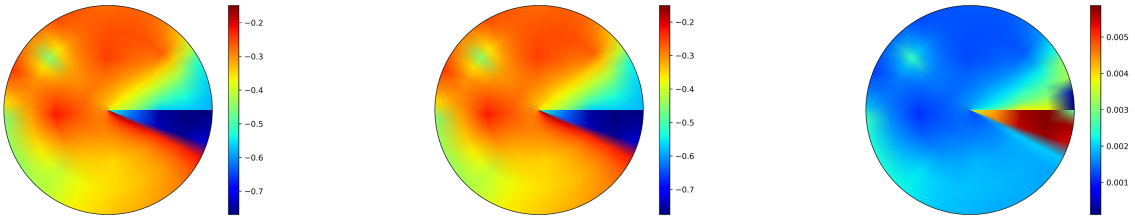

(a) Actual map (b) Estimated map (c) Absolute error map

Figure 2.12: Surface soil water content maps at 07:24 HRS on Day 5 in case 1.

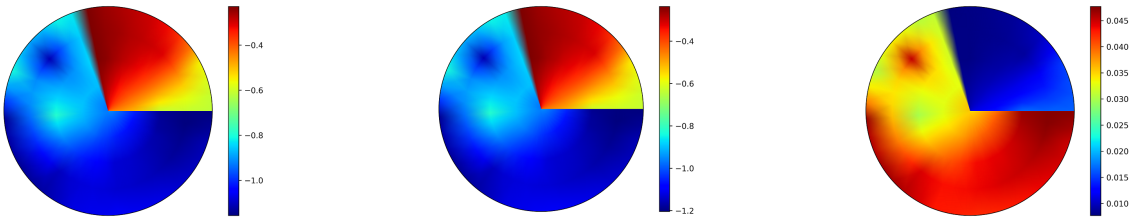

(a) Actual map (b) Estimated map (c) Absolute error map

Figure 2.13: Surface soil water content maps at 02:24 HRS on Day 2 in case 2.

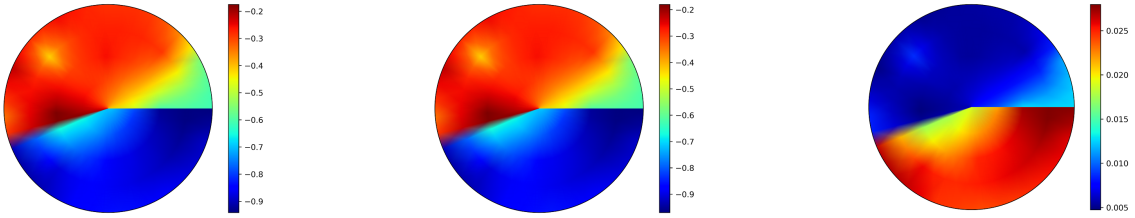

(a) Actual map (b) Estimated map (c) Absolute error map

Figure 2.14: Surface soil water content maps at 04:24 HRS on Day 3 in case 2.

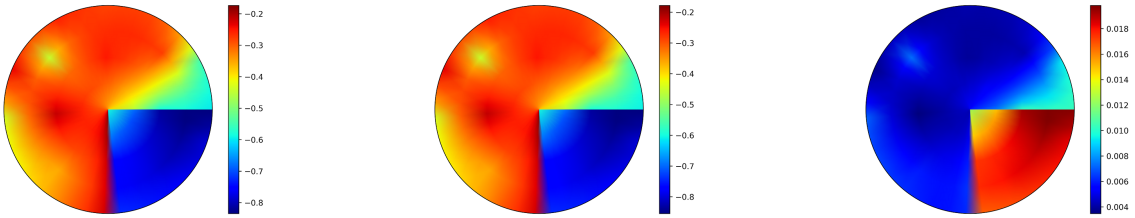

(a) Actual map (b) Estimated map (c) Absolute error map

Figure 2.15: Surface soil water content maps at 06:00 HRS on Day 4 in case 2.

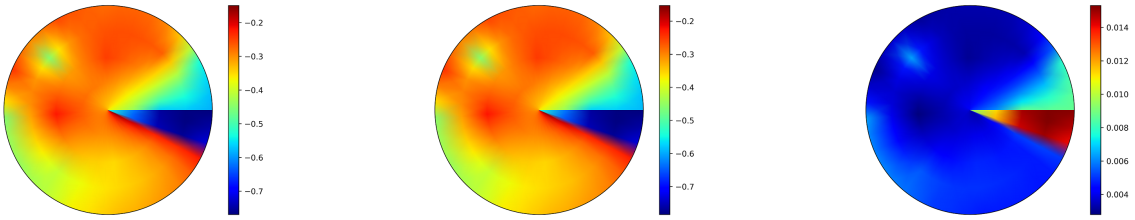

(a) Actual map (b) Estimated map (c) Absolute error map

Figure 2.16: Surface soil water content maps at 07:24 HRS on Day 5 in case 2.

In addition, Figures 2.13-2.16 indicate the soil water content maps at the same times for the surface of the field in case 2. By comparison Figures 2.9-2.12 to Figures 2.13-2.16, it can be seen that the absolute error maps in case 1 have smaller values compared to the absolute error maps in case 2 at the same times. Thus the EKF estimation with optimally sensor placement is able to provide more accurate soil water content maps.

2.6 Validation of Sensor Placement Using Real Data

In this section, we investigate the impact of optimal sensor placement in soil water estimation of the studied field using real collected data under different scenarios. The collected data includes the soil water tension of 14 locations at depth of 25 cm, 14 locations at depth of 50 cm, and 14 locations at depth of 75 cm. Before using the collected data as the measurements in the EKF, we have performed some preprocessing steps. First, we converted the soil water tension (Kpa) into the soil head pressure (m). Then, we normalized data using min-max normalization and transformed data between zero and one. It should be pointed out that normalized values are not allowed to be used in the model of the system, Equation (2.18). Thus in Richards' equation, we use the non-normalized values so that the model realizes how really dry or wet the field is. In addition, we analyzed the data set to determine which areas of the field have been irrigated over the time period of the experiment. Table 2.1 shows the amount and time of irrigation applied to the studied field over the time period.

Table 2.1: Irrigation amount and scheduling of the studied field.

Date	July 4	July 18	July 26	July 30	August 6
Amount (mm)	1.81	1.58	1.58	1.51	3.16

Within the simulation period at the sampling time without measurements, the soil moisture predictions are only provided by the field model. When the measurements are available, the head pressure measurements are assimilated into the field model using the EKF. Thus in the presence of the measurements, the soil moisture predictions provided by the field model are updated using the new measurements in the EKF. Because of the poor knowledge of the initial state values in the actual application, a wider range of the initial conditions is selected in the real data case. Thus in the following simulation, the initial guess of the state is considered as a random value between -6 m and -5 m. Two scenarios are constructed based on the availability of the number of actual measurements in the studied field.

2.6.1 Scenario 1: In Presence of Two Measurements

In the first scenario, we consider only two sensors in the field. Thus in the update step of EKF, there are only two measurements to correct the prediction values. To observe the effect of sensor placement on the performance of state estimation, we construct two cases. In case 1, the location of the sensor is determined based on the optimal sensor placement result while in case 2, the sensor position is selected randomly. Thus, in the first case, x_2 and x_{213} with the highest degree of observability among the measurement nodes are selected as the location of the sensors and in the second case, the sensors are placed at x_{3393} and x_{3542} with a lower degree of observability.

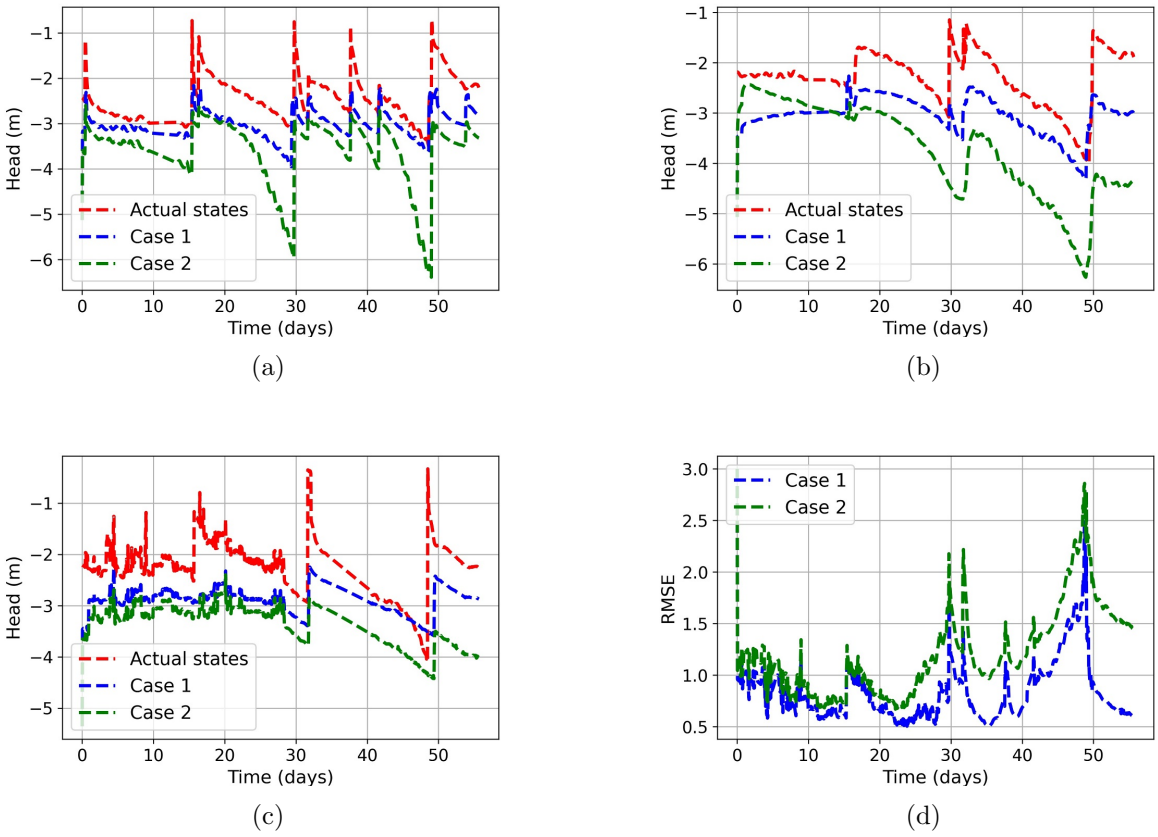

Figure 2.17: Estimation results using real data in Scenario 1. (a)-(c) Trajectories of the real states (red lines), estimated states in case 1 (blue lines), and estimated states in case 2 (green lines) at depth of (a) 25 cm, (b) 50 cm, and (c) 50 cm, below the surface. (d) Evolution of the RMSE of the original state vector during the simulation time in case 1 (blue lines) and case 2 (green lines).

Figure 2.17 shows the trajectories of the real states (red dash-dot) and estimated states (blue, green dash-dot) at some validation points. From Figures 2.17, it can be seen that the estimates by placing the sensors with higher degree of observability (case 1) converge faster to the actual states. Figure 2.17(d) compares the total estimation error between case 1 and case 2 and it demonstrates the RMSE in case 1 is smaller than case 2 over the simulations. Also, the average NRMSE over 50 days simulation in case 1, 30.75%, is much smaller than case 2, 44.56%.

2.6.2 Scenario 2: In Presence of a Few Measurements

In the second scenario, we consider a few sensors in the studied field. Thus there are more measurements in the EKF to update the soil moisture predictions. To verify the effectiveness of the proposed method, two cases are constructed. In case 1, of 42 data points, 15 measured nodes with a higher degree of observability, around 0.8607, are considered as the measurements in EKF. While, in case 2, another 15 measured nodes with a lower degree of observability, about 0.3734, are used as the training points. Also, the rest of the measurements are treated as validation points to compare the real states with estimated states in cases 1 and 2. Figure 2.18 represents the trajectories of the real states and EKF estimated states at some validation points. From Figure 2.18, firstly it can be seen that, by increasing the number of measurements in the second scenario, the performance of state estimation is improved. In addition, based on Figure 2.18, the performance of the state estimation is significantly improved in case 1 where there are measurements with a higher degree of observability, compared to case 2 that the measurements have a lower degree of observability. Figure 2.18(d) compares the total estimation error between case 1 and case 2 and it demonstrates the RMSE in case 1 is smaller than case 2 over the simulations. Also, the average NRMSE over 50 days simulation in case 1, 17.11%, is much smaller than case 2, 27.65%. Therefore, state estimation with optimally sensor placement is able to provide more accurate estimates in the actual application.

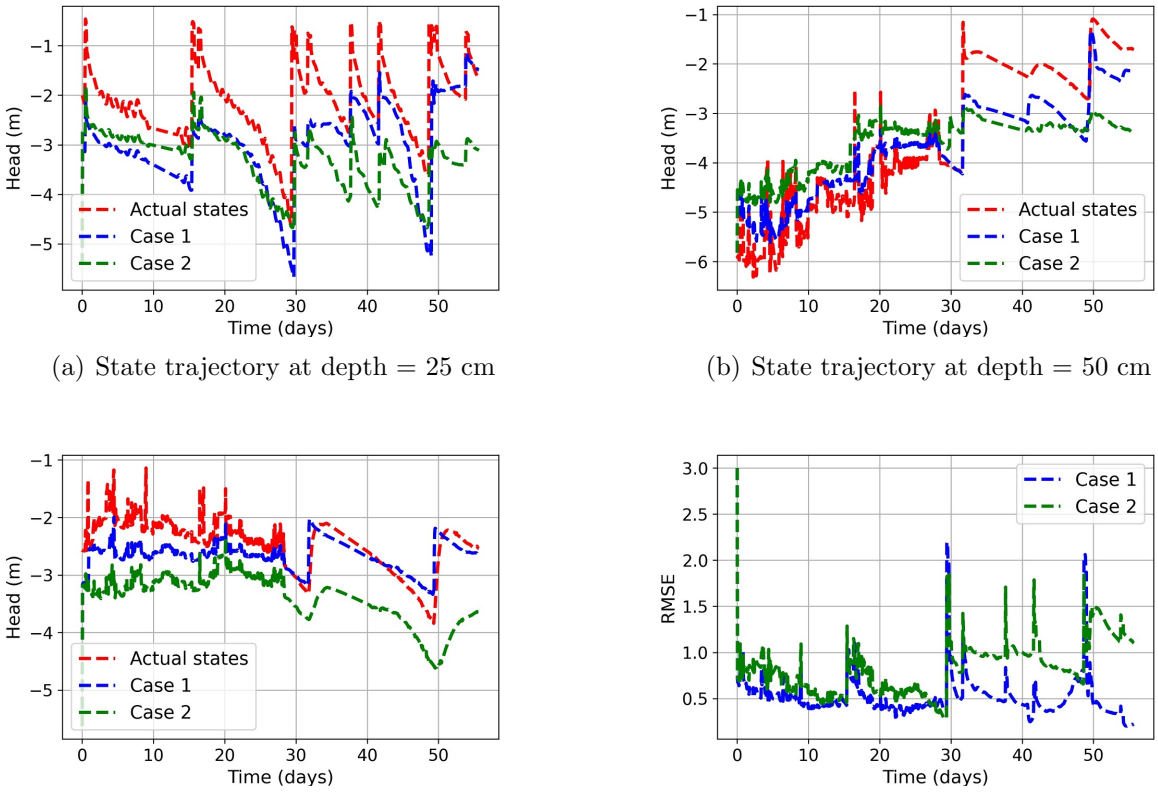

(a) State trajectory at depth = 25 cm

(b) State trajectory at depth = 50 cm

(c) State trajectory at depth = 75 cm

(d) Total estimation error trajectory

Figure 2.18: Estimation results using real data in Scenario 2. (a)-(c) Trajectories of the real states (red lines), estimated states in case 1 (blue lines), and estimated states in case 2 (green lines) at depth of (a) 25 cm, (b) 50 cm, and (c) 75 cm, below the surface. (d) Evolution of the RMSE of the original state vector during the simulation time in case 1 (blue lines) and case 2 (green lines).

In the end, we compare the simulation case study and real data case over the same simulation days using the average normalized RMSE. The NRMSE in the simulation study for case 1 (optimally placed sensors) and case 2 (sensors with a lower degree of observability) over 10 days simulation is about 13.69% and 25.70% respectively, while NRMSE in the real data study for cases 1 and 2 is respectively 17.36% and 26.12%, over the same simulation days. These comparisons demonstrate that optimal sensor placement can significantly improve the performance of state estimation in the actual application and the amount of improvement in the real data case study is very similar to the simulation study case.

2.7 Summary

In this chapter, the impact of optimal sensor placement in soil water estimation of an actual field was investigated. The agricultural field studied in this work was described and information on experiments and collected real data was provided. The three-dimensional agro-hydrological system with heterogeneous soils was developed to model the studied field. The Kriging interpolation method was implemented to obtain the heterogeneous soil parameters of the studied field. The modal degree of observability was applied to the field to determine the optimal sensor placement. The EKF was employed to estimate the soil water content of the studied field. The results obtained in the simulated case study confirmed that the estimates by placing the sensors with higher degree of observability converge faster to the actual states. The real case study demonstrated the performance of state estimation with optimally sensor placement is significantly improved in the actual applications.

Chapter 3

Simultaneous Soil Moisture and Soil Hydraulic Parameters Estimation

In this chapter, we propose a systematic procedure to simultaneously estimate the soil moisture and soil hydraulic parameters for large-scale three dimensional agro-hydrological systems with heterogeneous soils and changing measurements. We first introduce the investigated system and the formulation of the mathematical model in Section 3.1. Section 3.2 proposes the simultaneous estimation procedure. The key steps of the proposed procedure include augmented system construction, sensitivity analysis, variable selection, simultaneous state and parameter estimator, and parameters interpolation. The proposed method is applied to a simulated three dimensional field with heterogeneous soils under two different scenarios in Section 3.3. The simulation results of the considered agro-hydrological system illustrate the applicability and effectiveness of the proposed method on the performance of soil moisture estimation. Section 3.4 provides a summary of the work covered in this chapter.

3.1 System Description and Problem Formulation

Similar to Chapter 2, the 3D agro-hydrological system which has spatially heterogeneous soil parameters, is considered as the investigated system in Chapter 3. Essentially, the modeling described in Chapter 2 is used in this chapter. While some features of the investigated system are different in this chapter.

In Chapter 2, once the interpolated soil hydraulic parameters of the entire field are obtained from the soil texture analysis, the soil parameters of the model are considered to be constant during simulations. Thus, the model soil parameters at each step of simulation are the same as the initial guess ones. However, the soil hydraulic parameters may change over time and consequently, considering the soil hydraulic parameters constant during long-term simulations is not consistent with reality. Therefore, in this chapter, we propose to estimate the soil hydraulic parameters online and along with the soil moisture at the same time.

Figure 3.1: Microwave remote sensors on a central pivot.

In Chapter 2, the ground point sensors are used to provide the soil water content information of the field. The location of the measurements in this type of sensor is fixed. While in Chapter 3, the microwave soil moisture sensors are considered. Microwave remote sensors are mounted on the center pivots as shown in Figure 3.1. The center pivot system irrigates the field in a circular pattern around a central pivot. As the center pivot rotates, microwave sensors measure the surface soil moisture content of the irrigated locations. Thus, as the center pivot irrigates the field, the surface soil moisture at different locations are measured. Consequently, in this type of sensor, the measurements are changing. This is the second difference between this chapter and Chapter 2. More information about microwave remote sensors is provided in [1].

As has already been mentioned, in order to describe the dynamics of the water in the soil in an agro–hydrological system that is equipped with a center pivot irrigation system, we use the three-dimensional cylindrical coordinates version of the Richards equation due to its ability to account for the circular movement of the center pivot as follows [1]:

$$C(h)\frac{\partial h}{\partial t} = \frac{1}{r}\frac{\partial}{\partial r}\left[rK(h)\frac{\partial h}{\partial r}\right] + \frac{1}{r}\frac{\partial}{\partial \theta}\left[\frac{K(h)}{r}\frac{\partial h}{\partial \theta}\right] + \frac{\partial}{\partial z}\left[K(h)\left(\frac{\partial h}{\partial z}+1\right)\right] - S \qquad (3.1)$$

In the Richards equation, the soil hydraulic parameters are the saturated hydraulic conductivity K_s ($\frac{m}{s}$), saturated soil moisture θ_s ($\frac{m^3}{m^3}$), residual soil moisture θ_r ($\frac{m^3}{m^3}$), and curve-fitting soil hydraulic properties α ($\frac{1}{m}$) and n. For one type of soil, the parameter set $(K_s, \theta_s, \theta_r, \alpha, n)$ characterizes the properties of the soil. Each type of soil has its own set of soil parameters. In this study, a field with heterogeneous soils is considered such that the set of soil parameters at each node of the field varies.

To solve Equation (3.1) numerically, the same model development, spatial discretization, and ODEs integration considered in Chapter 2, are used in this chapter. The continuous-time

state-space representation of the field model can be expressed as:

$$\begin{aligned} \dot{x}(t) &= f\left(x(t), u(t), p\right) + \omega(t) \\ y(t) &= h\left(x(t), t, p\right) + v(t) \end{aligned} \tag{3.2}$$

where $x(t) \in \mathbb{R}^{N_x}$ represents the state vector containing N_x pressure head values for the corresponding spatial nodes. $u(t) \in \mathbb{R}^{N_u}$ and $p \in \mathbb{R}^{N_p}$ represent the input vector which is a collection of irrigation rates at all the nodes of the top surface and the parameter vector, respectively. Specifically, the parameter vector p represents the collection of the soil hydraulic parameters $[K_s, \theta_s, \theta_r, \alpha, n]$ of each spatial node. $y(t) \in \mathbb{R}^{N_y}$ denotes the measurement vector which is the volumetric soil moisture observation obtained from the microwave sensors. $\omega(t) \in \mathbb{R}^{N_x}$ and $v(t) \in \mathbb{R}^{N_y}$ represent the model disturbances and measurement noise. As outlined earlier, as the center pivot irrigates the field, the microwave radiometers measure the soil moisture content. Thus, during the rotation cycle of the center pivot, the irrigated locations and subsequently, the measured states are changing. This explains the explicit dependence of the output function $h(\cdot)$ on time.

3.2 Proposed Simultaneous State and Parameter Estimation Procedure

In this section, we propose the systematic method to estimate the soil moisture and soil hydraulic parameters of 3D agro-hydrological models simultaneously. Firstly, we create an augmented model with all the parameters augmented as additional states. In this global augmented model, the augmented states include both the original states and all the soil hydraulic parameters. Due to the unobservability of the augmented model, all elements of the augmented states can not be estimated at the same time. Thus in the proposed method, at a sampling time, only a subset of parameters are estimated along with original states

simultaneously based on the available measurements at the sampling time. Note that in the proposed method, the rest of the soil hydraulic parameters which are required in the augmented model, are interpolated using the estimated parameters at the sampling time.

To determine the subset of the parameters for simultaneous estimation, sensitivity analysis is employed in the proposed method. For simplification, we perform the sensitivity analysis offline. By applying the sensitivity analysis to the augmented model, the subset of the parameters that can be estimated at each sampling time is determined based on the available measurements at the sampling time. Since in this work, we assume the measuring locations are known at each sampling time prior to the estimation, it is possible to do the sensitivity analysis offline. Thus in this work, for each sampling time during estimation, the subset of parameters that can be estimated has been already specified prior to performing the estimation. While in actual applications when the measurements or their locations are available online, the sensitivity analysis needs to be performed online.

In the last step, based on the sensitivity analysis results, only the estimable parameters and the original states are updated in the EKF to perform state and parameter estimation. After updating the original states and the subset of parameters, we use the Kriging interpolation method to update the rest parameters that are not estimated at the sampling time. This procedure will be performed at each sampling time. The key steps of the proposed procedure are explained below.

3.2.1 Augmented System Construction

The first step for simultaneous state and parameter estimation of the system (3.2) is to augment the parameters as extra states and add the parameter vector to the end of the state vector in order to create an augmented state vector, $x_a = [x^T, p^T]^T$. This method is a rather standard approach to estimate state and parameter at the same time [13, 28]. The

parameter dynamics function is defined as:

$$\dot{p}(t) = 0 \tag{3.3}$$

By augmenting the system of equations in (3.2) with the parameter equation in (3.3), the following augmented system can be obtained:

$$\begin{aligned} \dot{x}_a(t) &= f_a(x_a(t), u(t)) + \omega_a(t) \\ y(t) &= h_a(x_a(t), t) + v(t) \end{aligned} \tag{3.4}$$

where $x_a(k) \in \mathbb{R}^{N_x+N_p}$, $w_a(k) \in \mathbb{R}^{N_x+N_p}$ denote the augmented state and model disturbance vectors, respectively. $f_a(\cdot)$ and $h_a(\cdot)$ denote the augmented state and output equations, respectively. An estimation of the augmented state x_a results in estimating the states and parameters of the original system at the same time.

3.2.2 Sensitivity Analysis

According to [11], the original nonlinear system (3.2) is observable and all original states can be estimated using a few measurements. However, after augmenting the original system with all parameters, the entire system may not be observable which leads to the issue that all states and all parameters can not be estimated at the same time. Since the unobservability of the augmented system is due to the augmentation of the parameters into the state vector, it is necessary to determine which parameters are identifiable and can be estimated with the states simultaneously. In [28], this issue has been addressed by performing the sensitivity analysis. It was demonstrated that the sensitivity analysis tells us how many parameters and which subset of parameters can be estimated with the states simultaneously. Thus, the sensitivity analysis plays a key role in the simultaneous state and parameter estimation and we will use this approach in this study.

The sensitivity analysis measures how the initial state $x(0)$ and the parameters p of the

system influence the outputs of the system. The sensitivity matrix, at time instant k, shown below contains the sensitivity of the outputs with respect to the initial states, $S_{y,x_0}(k) = \frac{\partial y(k)}{\partial x(0)}$ and the sensitivity of the outputs with respect to the parameters, $S_{y,p}(k) = \frac{\partial y(k)}{\partial p}$.

$$S_y(k) = \left[\begin{array}{cccc|ccc} \frac{\partial y_1}{\partial x_{a,1}(0)} & \frac{\partial y_1}{\partial x_{a,2}(0)} & \cdots & \frac{\partial y_1}{\partial x_{a,N_x}(0)} & \frac{\partial y_1}{\partial x_{a,N_x+1}(0)} & \cdots & \frac{\partial y_1}{\partial x_{a,N_x+N_p}(0)} \\ \frac{\partial y_2}{\partial x_{a,1}(0)} & \frac{\partial y_2}{\partial x_{a,2}(0)} & \cdots & \frac{\partial y_2}{\partial x_{a,N_x}(0)} & \frac{\partial y_2}{\partial x_{a,N_x+1}(0)} & \cdots & \frac{\partial y_2}{\partial x_{a,N_x+N_p}(0)} \\ \vdots & \vdots & \vdots & \vdots & \vdots & \vdots & \vdots \\ \frac{\partial y_{N_y}}{\partial x_{a,1}(0)} & \frac{\partial y_{N_y}}{\partial x_{a,2}(0)} & \cdots & \frac{\partial y_{N_y}}{\partial x_{a,N_x}(0)} & \frac{\partial y_{N_y}}{\partial x_{a,N_x+1}(0)} & \cdots & \frac{\partial y_{N_y}}{\partial x_{a,N_x+N_p}(0)} \end{array}\right]\Bigg|_k$$

The detailed steps to derive the sensitivity matrix are explained in [13]. The sensitivity matrix $S_y(k)$ is obtained based on the available measurements at time instant k. In fact, the sensitivity matrix $S_y(k)$ contains the information of the available measurements at the sampling time k. If the measured states change in the next sampling time $k+1$ then the information inside the sensitivity matrix will also change and consequently, information inside $S_y(k+1)$ will be different from the information of the matrix $S_y(k)$. Thus, the sensitivity matrices with the same measured states contain similar information. In the proposed method we consider two types of measurements and explain how the sensitivity analysis should be performed in each case.

3.2.2.1 Fixed Measured States

In the first case, we consider the systems in which the measured states are fixed. A field with ground point sensors is an example of this case in which the sensor positions and subsequently the measuring locations are fixed. Thus all sensitivity matrices obtained during simulation contain similar information. This case has already been studied in [28]. Based on [28], in this type of system, after obtaining the sensitivity matrix at each sampling time, we collect all $S_y(k)$ from time t_0 to time t_n to obtain the following sensitivity matrix:

$$S_y(t_0,\ldots,t_n,x_a)=\begin{bmatrix} \frac{\partial y_1(t_0)}{\partial x_{a,1}(0)} & \cdots & \frac{\partial y_1(t_0)}{\partial x_{a,N_x+N_p}(0)} \\ \vdots & & \vdots \\ \frac{\partial y_{N_y}(t_0)}{\partial x_{a,1}(0)} & \cdots & \frac{\partial y_{N_y}(t_0)}{\partial x_{a,N_x+N_p}(0)} \\ \vdots & & \vdots \\ \frac{\partial y_1(t_n)}{\partial x_{a,1}(0)} & \cdots & \frac{\partial y_1(t_n)}{\partial x_{a,N_x+N_p}(0)} \\ \vdots & & \vdots \\ \frac{\partial y_{N_y}(t_n)}{\partial x_{a,1}(0)} & \cdots & \frac{\partial y_{N_y}(t_n)}{\partial x_{a,N_x+N_p}(0)} \end{bmatrix}$$

In [28, 58], it is shown that the sensitivity and observability of the system are related to each other and a full rank sensitivity matrix with a low condition number is a sufficient condition for full observability and simultaneous all states and parameters estimation. In case the sensitivity matrix is not full rank, the augmented system is not fully observable and all elements of the augmented state vector x_a can not be estimated simultaneously. Thus, calculating the rank of the matrix $S_y(t_0,\ldots,t_n,x_a)$ represents how many elements of x_a can be estimated at the same time. Specifically in the proposed method, to calculate the rank of the sensitivity matrix, we use the singular value decomposition (SVD) tool which is a well-known method to calculate the rank of large-scale matrices with high accuracy. SVD writes the matrix as a sum of equally sized matrices that decrease in dominance (or singular value σ_i) as

$$S_y(t_0,\ldots,t_n,x_a)=u_1\sigma_1v_1^T+\cdots+u_q\sigma_qv_q^T \tag{3.5}$$

Once the decomposition of the sensitivity matrix $S_y(t_0,\ldots,t_n,x_a)$ is obtained, determining the rank of the sensitivity matrix is equivalent to determine the number of non-zero singular values. In fact, if for some $k\leq q, \sigma_k=\cdots=\sigma_q=0$, then the sensitivity matrix is rank deficient and k value is the matrix rank [58]. To determine zero singular values more precisely, plotting the singular values with respect to the parameter index in a logarithmic scale is suggested. The biggest gap in this plot represents the rank of the given matrix [58].

Note that in systems with fixed measured states, obtaining the rank of $S_y(t_0,\ldots,t_n,x_a)$

is sufficient to represent how many elements of x_a can be estimated simultaneously at all sampling times. In fact, the number of elements of x_a that can be estimated at each sampling time is the same. In case of a rank deficient sensitivity matrix $S_y(t_0, \ldots, t_n, x_a)$, we need to determine which elements of the augmented state have the most important effect on the outputs and should be selected for estimation. To achieve this objective, Liu et al. [28] proposed to use the orthogonalization method. They demonstrated the orthogonalization method is able to select the most appropriate variables for simultaneous estimation by maximally extracting the information contained in the measured outputs. In this work, we use the orthogonalization algorithm presented in [28] to choose the most important parameter set for simultaneous state and parameter estimation. In the following, we summarize the algorithm.

The orthogonalization method specifies elements of x_a that have most impact on the output y by finding the strongly linearly independent columns in the sensitivity matrix $S_y(t_0, \ldots, t_n, x_a)$ in which each column corresponds to an element in x_a. Before conducting the variable selection, we should normalize the matrix $S_y(t_0, \ldots, t_n, x_a)$ with respect to the magnitudes of the different elements in x_a and form the normalized sensitivity matrix S_N. To detect the strongly linearly independent columns, we need to first find the column of S_N that has the biggest norm. Then, we estimate the information in the matrix S_N that can be expressed by the selected column and obtain the residual matrix by removing this information from the matrix S_N. Next, we select the column with the largest norm in the residual matrix and add it to the previously selected column in order to form a set of linearly independent columns. We repeat these steps to detect all the strongly linearly independent columns of the normalized sensitivity matrix which leads to the most important elements of augmented state vector for simultaneous estimation. More details on the orthogonalization method are explained in [28].

As has already been discussed, original states are observable and unobservability of the augmented model is due to the parameters augmentation. Thus in this work, we estimate

all original states at each sampling time and perform the variable selection only among the parameters. Consequently, once the sensitivity matrix $S_y(t_0, \ldots, t_n, x_a)$ is obtained, we first remove the information that can be expressed by all original states from the sensitivity matrix and then use the residual matrix which contains only the information of the parameters for rank calculation and determination of significant parameters.

3.2.2.2 Changing Measured States

In the second case, we consider systems in which the measured states are changing. A field that is equipped with center pivot and microwave remote sensors is such a case with changing measurements. Figure 3.2 shows a schematic representation of center pivots equipped with microwave sensors. In this field, during the rotation cycle of the center pivot, the irrigated locations and subsequently, the measuring locations are changing.

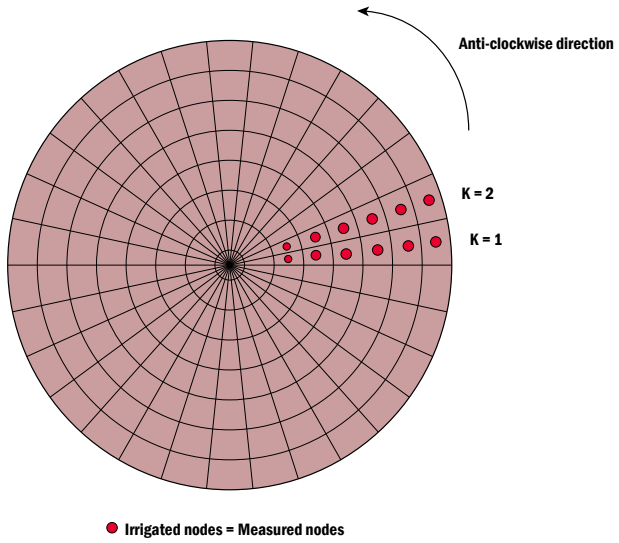

Figure 3.2: A schematic representation of center pivots equipped with microwave sensors.

For example, in the first sampling time, $k = 1$, when the center pivot irrigates the first sector of field, the measuring locations are the presently irrigated nodes (represented with the red dots at $k = 1$ in Figure 3.2). In the next sampling time, $k = 2$, as the center pivot moves to the second sector for irrigation, the measuring locations also change (red dots at $k = 2$

in Figure 3.2). In this type of systems, collecting all sensitivity matrices in one matrix is not appropriate. Because in this case, the sensitivity matrix computed at sampling time k contains the information of the available measurements at this step and by changing the measured states in the next sampling time, information of the sensitivity matrix will also change. Thus, only those sensitivity matrices which have the same measured states contain similar information and can be considered together. As a result, contrary to the fixed measurement case that we collect all sensitivity matrices in one matrix $S_y(t_0, \ldots, t_n, x_a)$ and investigate it, in the system with changing measured states, we propose to place all the sensitivity matrices of the same measured states together in one matrix and apply the variable selection to that matrix.

Let us take an example to explain the above procedure. Consider a field with changing measurements as an example. As the center pivot rotates and irrigates the field, the presently irrigated locations are considered as the measured nodes (represented with the red dots in Figure 3.2). Suppose that the whole field in the azimuthal direction is divided into 40 compartments. Figure 3.3 represents how we collect the sensitivity matrices in this field with rotating measurements. For example, for the first sector, the calculated sensitivity matrices of the first sector at the consecutive rotations are $S_y(1), S_y(41), S_y(81), \cdots$. All the sensitivity matrices of the first sector are collected in one matrix to form an overall sensitivity matrix of the first sector, S_y^1. Then, by calculating the rank of matrix S_y^1 and applying the variable selection to S_y^1, the estimable parameters for the case the measuring locations are in the first sector will be determined. The same procedure will be performed for all other sectors of the field to determine the most important parameters for simultaneous estimation at each sector. Therefore in a system with changing measurements, the subset of parameters for simultaneous estimation at each sampling time varies. Note that similar to the fixed measurement case, the SVD analysis and orthogonalization method respectively are used in this case to calculate the rank of the sensitivity matrices of each sector and determine the subset of parameters for estimation at each sector.

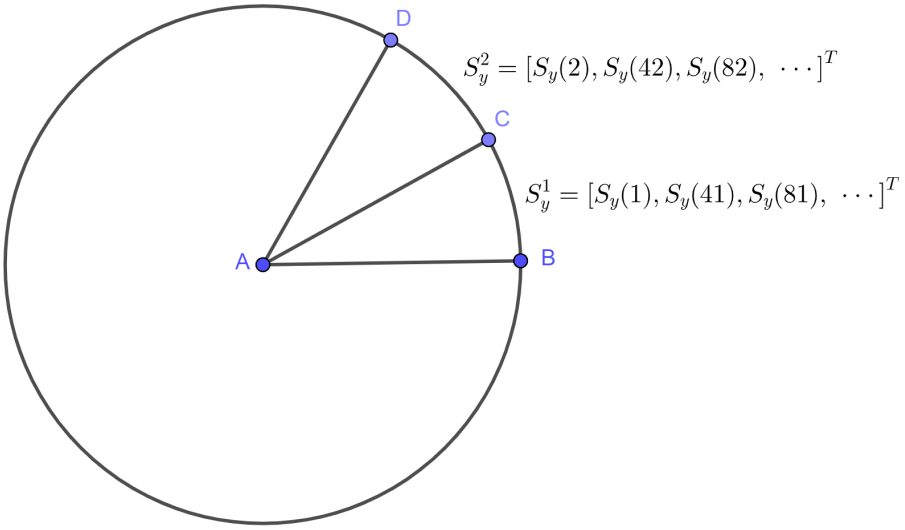

Figure 3.3: A schematic representation of how to collect sensitivity matrices when the measured states are changing.

3.2.3 Simultaneous State and Parameter Estimator

After applying the sensitivity analysis to the augmented model and determining the subset of parameters for simultaneous estimation, a state estimator is used to estimate the augmented state vector x_a. By estimating the augmented state of the augmented model, the states and parameters of the original model are estimated at the same time. In this work, we employ the discrete-time EKF to estimate the states of the augmented model in (3.6). The detailed steps are described as follows:

The continuous-time model of the augmented system (3.4) is discretized to obtain its discrete-time equivalent. The discrete-time version can be expressed as:

$$\begin{aligned} x_a(k+1) &= F_a(x_a(k), u(k)) + \omega_a(k) \\ y(k) &= H_a(x_a(k), k) + v(k) \end{aligned} \tag{3.6}$$

The augmented state vector x_a contains the original states $x(k) \in \mathbb{R}^{N_x}$ and all soil parameters $p(k) \in \mathbb{R}^{N_p}$. The parameter vector $p(k)$ consists of two different parameter sets: $p_e(k)$ and $p_r(k)$. $p_e(k)$ is the estimable parameter vector which is determined by the sensitivity analysis

and its elements will be estimated using EKF. $p_r(k)$ is the remaining parameter vector which includes the rest of the soil hydraulic parameters that are not estimated and will be constant during EKF estimation. However, the elements of this vector will be updated using Kriging interpolation at each sampling time after estimating the elements of $p_e(k)$. For fixed measurements, the soil parameters belong to the vectors $p_e(k)$ and $p_r(k)$ are constant, while in the case of changing measurements, $p_e(k)$ and $p_r(k)$ elements change at each sampling time.

In the first step of EKF, the filter is initialized with a guess of the augmented state $x_a(0)$ and its covariance matrix $P_a(0|0)$. Since all parameters are augmented in the augmented state vector x_a, we initially considered all the parameters in the construction of the covaraince matrix, $P_a \in \mathbb{R}^{(N_x+N_p)\times(N_x+N_p)}$. The next step of EKF is prediction. The new augmented state x_a and its covariance matrix P_a are predicted using the nonlinear model at time $t(k+1)$:

$$\hat{x}_a(k+1|k) = F_a(\hat{x}_a(k|k), u(k)) \tag{3.7}$$

$$P_a(k+1|k) = A(k)P_a(k|k)A(k)^T + Q \tag{3.8}$$

where $A(k) = \frac{\partial F_a}{\partial x_a}|_{\hat{x}_a(k|k),\ u(k)}$ and Q is the covariance matrix of the process disturbance ω_a. Note that, since we estimate only a subset of parameters at each sampling time and the values of unestimated parameters are assigned a constant value, the jacobians of the state and output equations with respect to the unestimated parameters at that sampling time are set to zero. Thus, the entries of $A(k)$ related to unestimated parameters are set to zero. Consequently, in Equation (3.8), the elements of the covariance matrix related to unestimated parameters will not be updated.

The last step of EKF is updating the predicted augmented state and its covariance matrix using the observation $y(k+1)$ at time $t(k+1)$ by:

$$\hat{x}_a(k+1|k+1) = \hat{x}_a(k+1|k) + G(k+1) \times [y(k+1) - H_a(\hat{x}_a(k+1|k))] \tag{3.9}$$

$$P_a(k+1|k+1) = [I - G(k+1)C(k+1)]P_a(k+1|k) \tag{3.10}$$

In the above equations, $G(k+1)$ is the Kalman gain matrix that can be calculated as:

$$G(k+1) = P_a(k+1|k)C^T(k+1) \times [C(k+1)P_a(k+1|k)C^T(k+1) + R]^{-1} \tag{3.11}$$

where $C(k+1) = \frac{\partial H_a}{\partial x_a}|_{\hat{x}_a(k+1|k)}$ and R is the covariance matrix of the measurement noise v. Similar to the prediction step, due to the constant values of the unestimated parameters, the entries of $C(k+1)$ related to unestimated parameters should set to be zero. $\hat{x}_a(k+1|k+1)$ is the estimated augmented state which includes the estimated original states and a subset of parameters. Then, we use the estimated parameters, as the measured values in the Kriging interpolation method in order to update the unestimated parameters. Thus, the unestimated parameter vector $p_r(k)$ is updated at each sampling time, using the Kriging interpolation, when the estimated parameter vector $p_e(k)$ is obtained. The whole estimated and interpolated parameter vector $p(k)$ is used in Equation (3.7).

3.3 Results

In this work, two different simulation case studies are constructed based on the various types of measured nodes and the size of the field in order to extensively study the performance of the proposed approach. In the following simulations, the root mean square error (RMSE) at a time instant and the average RMSE will be used to assess the estimation performance:

$$RMSE_{x_a}(k) = \sqrt{\frac{\sum_{i=1}^{n_{x_a}}(\hat{x}_{a,i}(k) - x_{a,i}(k))^2}{n_{x_a}}} \tag{3.12}$$

$$RMSE_{x_a} = \frac{\sum_{k=0}^{N_{sim}-1} RMSE_{x_a}(k)}{N_{sim}} \tag{3.13}$$

where $\text{RMSE}_{x_a}(k)$ with $k = 0, \cdots, Nsim - 1$ shows the evolution of the RMSE value over time and RMSE_{x_a} shows the average value.

3.3.1 Scenario 1: A Small Field with Fixed Measurements

A field of radius 50 m and depth of 0.30 m is investigated in the first scenario. We discretize the field into 6, 40, and 16 nodes in the radial, azimuthal and axial directions, respectively. The head pressure of the soil at these discretized nodes are the states of the system. A schematic diagram of the investigated field is shown in Figure 3.4.

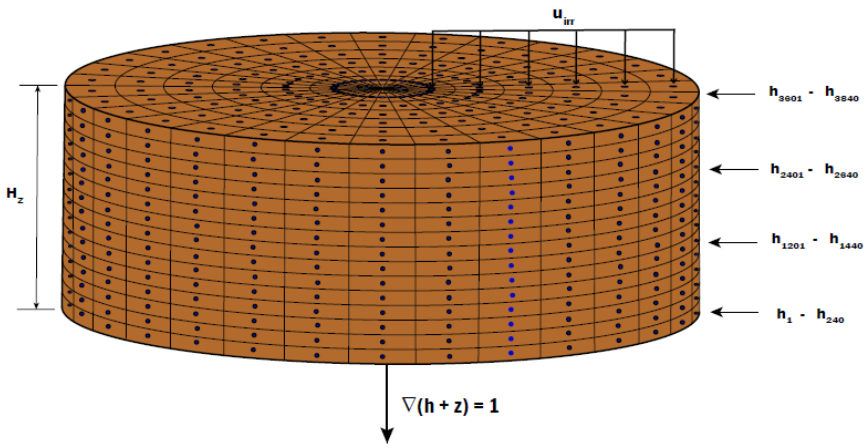

Figure 3.4: A schematic diagram of the investigated field [1].

Heterogeneous soils is considered in the investigated field. In fact, the set of soil parameters at each node of the surface of the field varies. The distribution of soil parameters on the surface is shown in Figure 3.5. The distribution of soil parameters at the lower layers of the field is the same as one on the surface. In addition, the initial condition of the head pressure (x_0) at each state is various and it comes from a random variable between -1.5 m and -1.35 m. The center pivot rotates at a speed of 0.011 m/s and the irrigation amount is a constant rate of 3.6 mm/day which is applied to the field surface in the first 8 hours of each day.

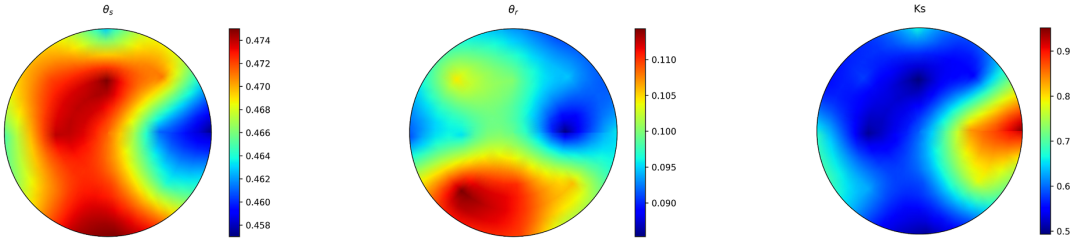

(a) saturated volumetric moisture content (θ_s (m^3m^{-3}))

(b) residual moisture content (θ_r (m^3m^{-3}))

(c) saturated hydraulic conductivity (K_s ($cmhr^{-1}$))

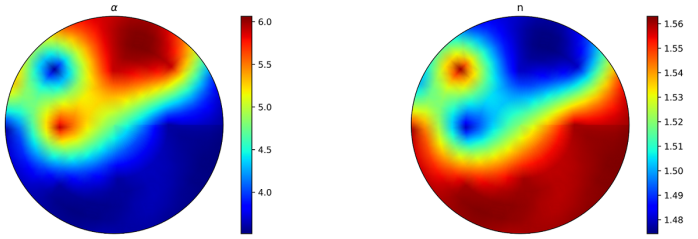

(d) curve-fitting soil hydraulic property (α (m^{-1}))

(e) Water Retention Model Parameter (n)

Figure 3.5: Heterogeneous distribution of soil parameters on the surface of the investigated field.

In this scenario, we directly measure the head pressure (h) of the soil which is the state of the system. Thus, the measurement vector $y(k)$ is the head pressure at the measured nodes of the field and the general output equation in (3.4) converts to the following equation that simply represents a matrix (C) indicating which states are measured by the sensors:

$$y(k) = Cx_a(k) + v(k) \tag{3.14}$$

In this scenario, the measuring locations are fixed. Thus, the matrix C is constant. In the following, we illustrate how the proposed estimation method may be used to estimate the head pressure and soil hydraulic parameters simultaneously while the fixed measurements are used.

3.3.1.1 Determination of Significant Parameters

The first step is to construct the augmented model. Based on the system discretization, there are in total 3840 states and 1200 parameters in the model. Specially, the parameter vector is:

$$p = [K_{s,1}, \theta_{s,1}, \theta_{r,1}, \alpha_1, n_1, \cdots, K_{s,240}, \theta_{s,240}, \theta_{r,240}, \alpha_{240}, n_{240}] \in \mathbb{R}^{1200}$$

and the state vector is:

$$x = [x_1, x_2, \cdots, x_{3840}]^T \in \mathbb{R}^{3840}$$

Thus, the augmented state vector x_a which contains 3840 original states and 1200 parameter states is as follows:

$$x_a = [x_1, \cdots, x_{3840}, K_{s,1}, \theta_{s,1}, \theta_{r,1}, \alpha_1, n_1, \cdots, K_{s,240}, \theta_{s,240}, \theta_{r,240}, \alpha_{240}, n_{240}]^T \in \mathbb{R}^{5040}$$

Six tensiometers are installed at different locations of the depth 30 cm below the surface in order to measure the head pressure values of the 180^{th}, 181^{th}, 182^{th}, 183^{th}, 184^{th}, 185^{th} states, respectively. Thus, the output vector is:

$$y = [x_{180}, x_{181}, x_{182}, x_{183}, x_{184}, x_{185}]^T \in \mathbb{R}^6.$$

The next step is to perform the sensitivity analysis in order to determine the most important parameters for simultaneous estimation. Based on the discussion in Section 3.2.2.1 and since the measuring locations are fixed in this scenario, we only need to calculate the sensitivity matrix at each sampling time $S_y(k)$ and form the sensitivity matrix $S_y(t_0, \cdots, t_n, x_a)$. The SVD of matrix $S_y(t_0, \cdots, t_n, x_a)$ is then computed to explore how many parameters can be estimated at each sampling time. Since there are 1200 parameters to be determined, there are 1200 columns in the matrix $S_y(t_0, \cdots, t_n, x_a)$. An SVD of this matrix then yields

1200 singular values $\sigma_1, \cdots, \sigma_{1200}$. These singular values are presented in Figure 3.6 on a logarithmic scale. The biggest gap between σ_{24} and σ_{25} of approximately 3.5 decades on the logarithmic scale, indicates a true zero for the 24^{th} singular value and, hence, a possible lack of observability. Thus, the rank of the sensitivity matrix is 24 which means, only 24 parameters can be simultaneously estimated with the original states at each sampling time.

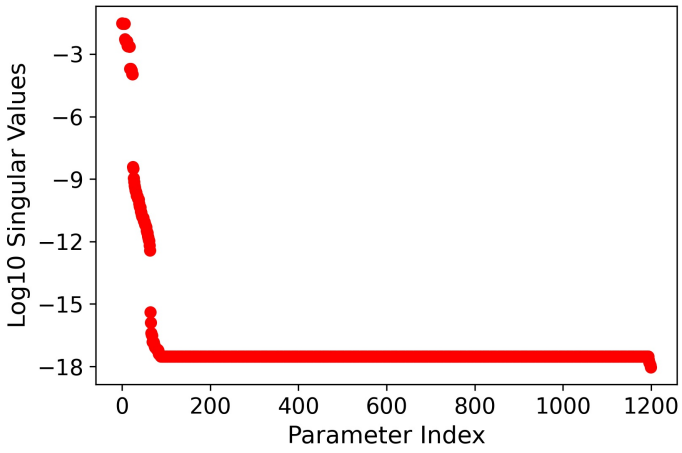

Figure 3.6: Singular values of the sensitivity matrix in scenario 1.

Afterward, we employ the orthogonalization method to select the most important 24 parameters for estimation. Based on the results of the orthogonalization method, the most significant parameters are K_s, θ_s, α, and n at 6 measured nodes (nodes 180^{th}, 181^{th}, $\cdots$, 185^{th}). Therefore, all original states and K_s, θ_s, α, and n parameters at 6 measured nodes should be estimated simultaneously in the EKF at each time instant and the rest of the parameters should be interpolated using the EKF estimated parameters. The final selected parameters for simultaneous state and parameter estimation in the first scenario are listed in Table 3.1.

Table 3.1: Selected parameters for estimation using orthogonalization method.

$K_{s,180}$	$\theta_{s,180}$	α_{180}	n_{180}	$K_{s,181}$	$\theta_{s,181}$	α_{181}	n_{181}
$K_{s,182}$	$\theta_{s,182}$	α_{182}	n_{182}	$K_{s,183}$	$\theta_{s,183}$	α_{183}	n_{183}
$K_{s,184}$	$\theta_{s,184}$	α_{184}	n_{184}	$K_{s,185}$	$\theta_{s,185}$	α_{185}	n_{185}

3.3.1.2 Estimation Results

The three dimensional agro-hydrological system with nominal soil parameters is used to simulate the model and obtain the head pressure of the actual system and is further used in the prediction step of EKF. The six head pressure measurements are used to correct the prediction state estimates in the update step of EKF at each sampling time. Process noise and measurement noise are considered in the simulations and they have zero mean and standard deviations of 1×10^{-6} and 6×10^{-2}, respectively. In EKF design, a 10% to 15% mismatch in the initial condition of the states and initial guess of the parameters is considered.

To verify the effectiveness of the proposed method, three different cases are considered. In case 1, only the states of the original system are estimated while there is uncertainty in the soil parameters. In case 2, without considering the sensitivity analysis, all 5040 variables in the augmented state are estimated. In case 3, the proposed method is used for simultaneous state and parameter estimation. In this case, at each sampling time, firstly the original states and a set of twenty-four parameters selected from the sensitivity analysis are estimated simultaneously, and then, the rest of the parameters are interpolated using twenty-four estimated parameters. The estimation results of the three cases are shown in Figure 3.7. From Figure 3.7, it can be seen that the estimation performance in case 1 and case 2 are much poorer compared with case 3. The poor estimation performance of case 1 is due to the uncertainty in all parameters that are not estimated. In case 2, because of the unobservability of the entire augmented state vector x_a, the performance of estimation is poor. Based on Figure 3.6, the sensitivity matrix is not full rank which implies that the augmented system is not fully observable and all elements of x_a can not be estimated at the same time. Thus, estimating all elements of x_a without considering the observability may lead to overfitting the outputs and poor state estimation performance as shown in case 2.

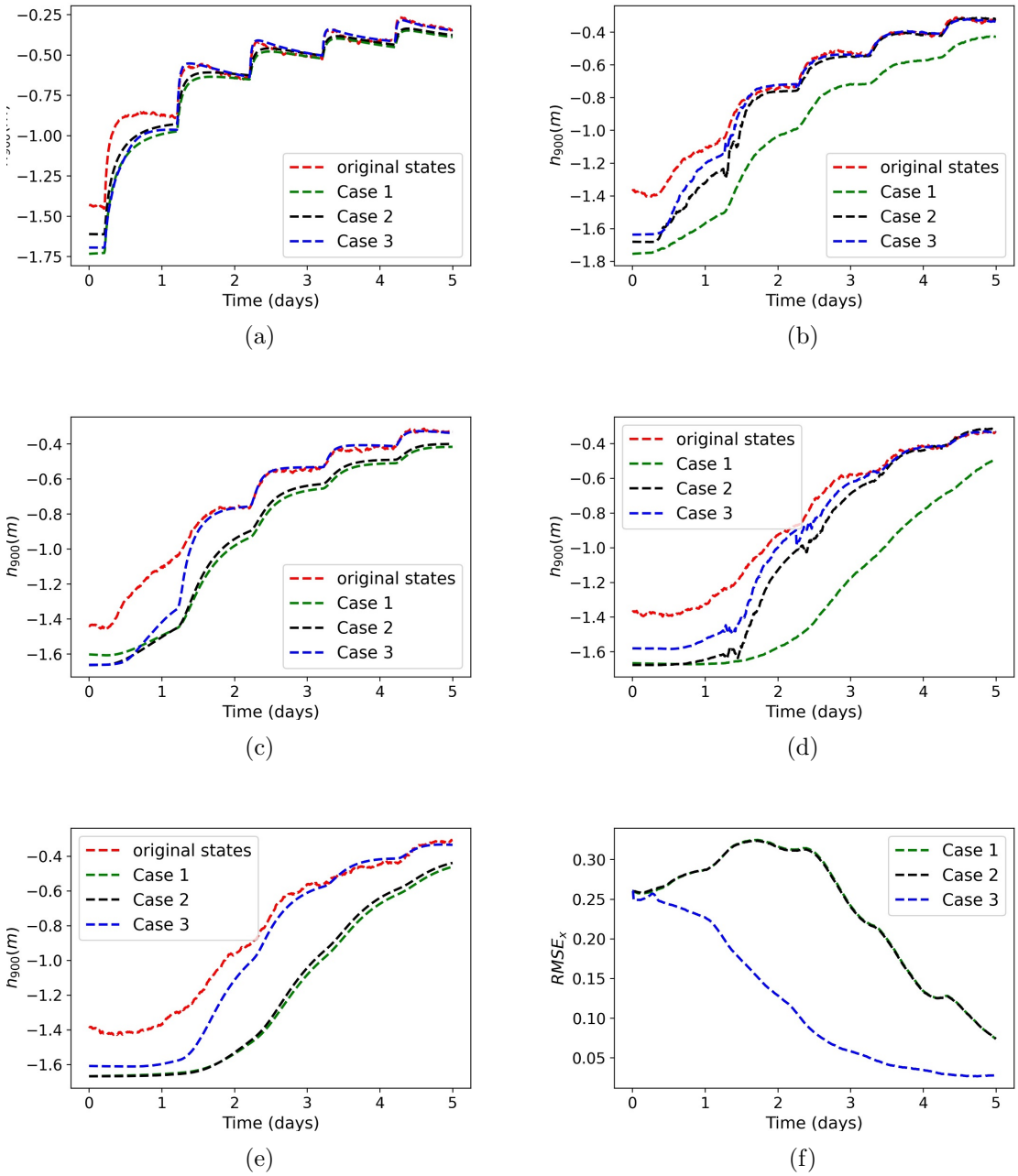

Figure 3.7: (a)-(e) Trajectories of the actual states (red lines), estimated states in Case 1 (green lines), estimated states in Case 2 (black lines), and estimated states in Case 3 (blue lines). (f) Evolution of the RMSE of the original state vector during the simulation time in Case 1 (red lines), Case 2 (blue lines) and Case 3 (black lines).

In case 3, the observability information is taken into account and only a subset of soil hydraulic parameters that are selected by the sensitivity analysis is estimated along with

original states simultaneously. Interpolating the unestimated parameters using the estimated parameters is another feature of this case that improves the performance of estimation. The improved estimation performance in case 3 can be further seen from Table 3.2, which shows the average performance indexes for the entire simulation of the three cases. From Table 3.2, it can be seen that the average RMSE of the state vector, parameter vector, and entire augmented state vector in case 3 are smaller than case 1 and case 2.

Table 3.2: The average performance indexes for the entire simulation in scenario 1.

	$RMSE_x$	$RMSE_p$	$RMSE_{x_a}$
Case 1	24.90%		
Case 2	24.19%	17.66%	24.69%
Case 3	14.25%	14.99%	14.27%

3.3.2 Scenario 2: A Larger Field with Rotating Measurements

In the second scenario, we consider a comparatively bigger field than the first scenario. The radius of the field is 290 m and 0.3 m depth is investigated. The entire system is discretized into 12000 nodes with 30, 40, and 10 nodes in the radial, azimuthal and axial directions, respectively. Contrary to the system considered in scenario 1, in the system considered in scenario 2, we use microwave remote sensors to provide the soil water information of the field. Microwave remote sensors measure the soil moisture content of the presently irrigated locations on surface of the field. Thus, the measuring locations are changing in this scenario. The heterogeneous soil hydraulic parameters values, the rotation speed of the center pivot, the irrigation scheduling and amount by the center pivot, and other simulation settings are the same as the one considered in scenario 1.

3.3.2.1 Determination of Significant Parameters

According to the system discretization, there are in total 12000 states and 6000 parameters in the model. Thus, the augmented state x_a has 18000 elements as follows:

$$x_a = [x_1, \cdots, x_{12000}, K_{s,1}, \theta_{s,1}, \theta_{r,1}, \alpha_1, n_1, \cdots, K_{s,1200}, \theta_{s,1200}, \theta_{r,1200}, \alpha_{1200}, n_{1200}]^T \in \mathbb{R}^{18000}$$

Based on Section 3.2.2.2 and since the rotating measurements are considered in this scenario, the sensitivity matrices of the sectors with the same measuring locations should be placed together in order to determine the estimable parameters for that sectors. Since there are 6000 parameters to be determined, there are 6000 columns in the sensitivity matrix. An SVD of this matrix then yields 6000 singular values $\sigma_1, \cdots, \sigma_{6000}$.

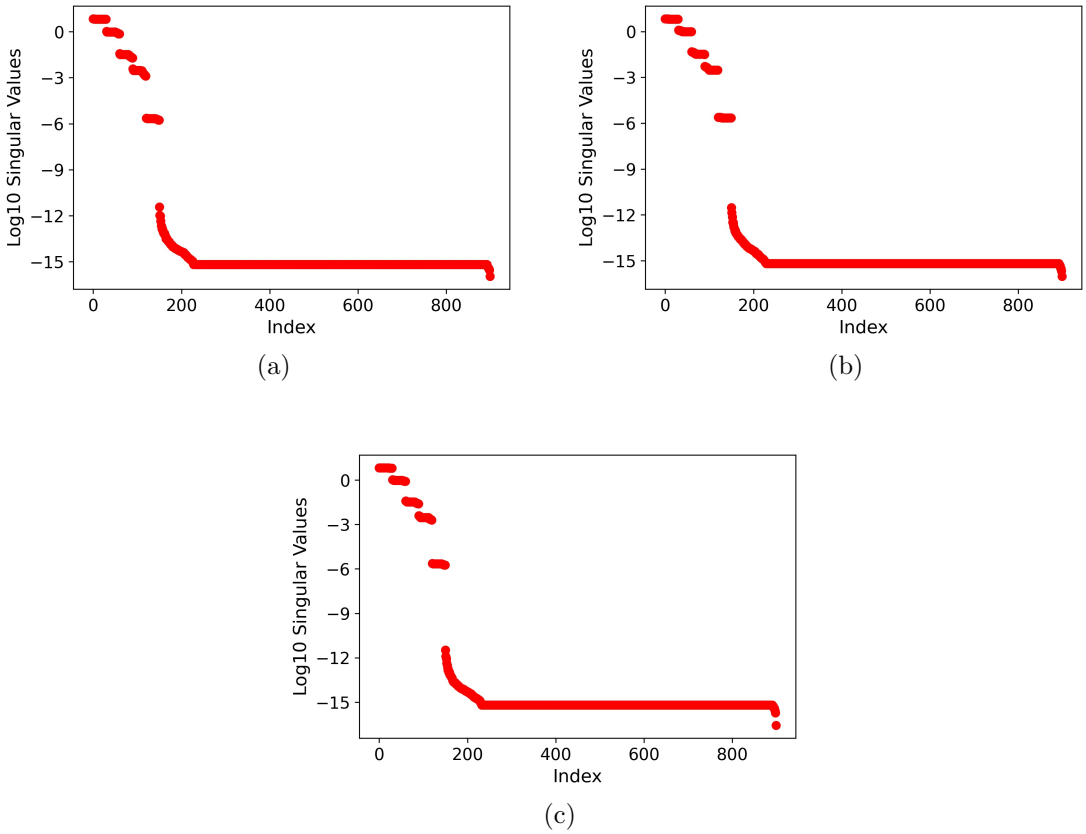

Figure 3.8: Singular values of sensitivity matrix in scenario 2 at (a) 1^{st} sector; (b) 10^{th} sector; (c) 25^{th} sector.

The singular values of the overall sensitivity matrices for some selected sectors of the field are presented in Figure 3.8 on a logarithmic scale. In all subplots of Figure 3.8, a clearly visible gap between σ_{150} and σ_{151} of approximately 5.8 decades on the logarithmic scale, indicates a true zero for the 150^{th} singular value and, hence, a possible lack of observability. Thus, in the selected three sectors, the rank of the sensitivity matrix is 150 which means, of total 6000 parameters, only 150 parameters can be estimated with the states at these sampling times. The same results are obtained for other sectors of the field. Next, we employ the orthogonalization method to select the most important 150 parameters for estimation. Based on the results of the orthogonalization method, at the sampling time k, the estimable parameters are $K_s, \theta_s, \theta_r, \alpha$, and n corresponding to the measured nodes in the sampling time k. Therefore, at each sampling time, all original states and $K_s, \theta_s, \theta_r, \alpha$, and n at 30 measured nodes should be estimated in the proposed method.

3.3.2.2 Estimation Results

Similar to scenario 1, three different cases are considered to study the effectiveness of the proposed method on the estimation performance in this scenario. Case 1 is only soil moisture estimation with uncertainty in the soil hydraulic parameters. Case 2 estimates all soil moisture and soil hydraulic parameters without considering the sensitivity analysis. In case 3, the proposed method is used for simultaneous soil moisture and soil hydraulic parameter estimation. The thirty soil moisture measurements are used to correct the prediction estimates in the update step of EKF at each sampling time. In EKF design, a 10% to 15% mismatch in the initial condition of the states and initial guess of the parameters is considered. The estimation results of the three cases are shown in Figure 3.9. From Figure 3.9, it can be seen that the estimation performance in case 3 is much improved compared to cases 1 and 2.

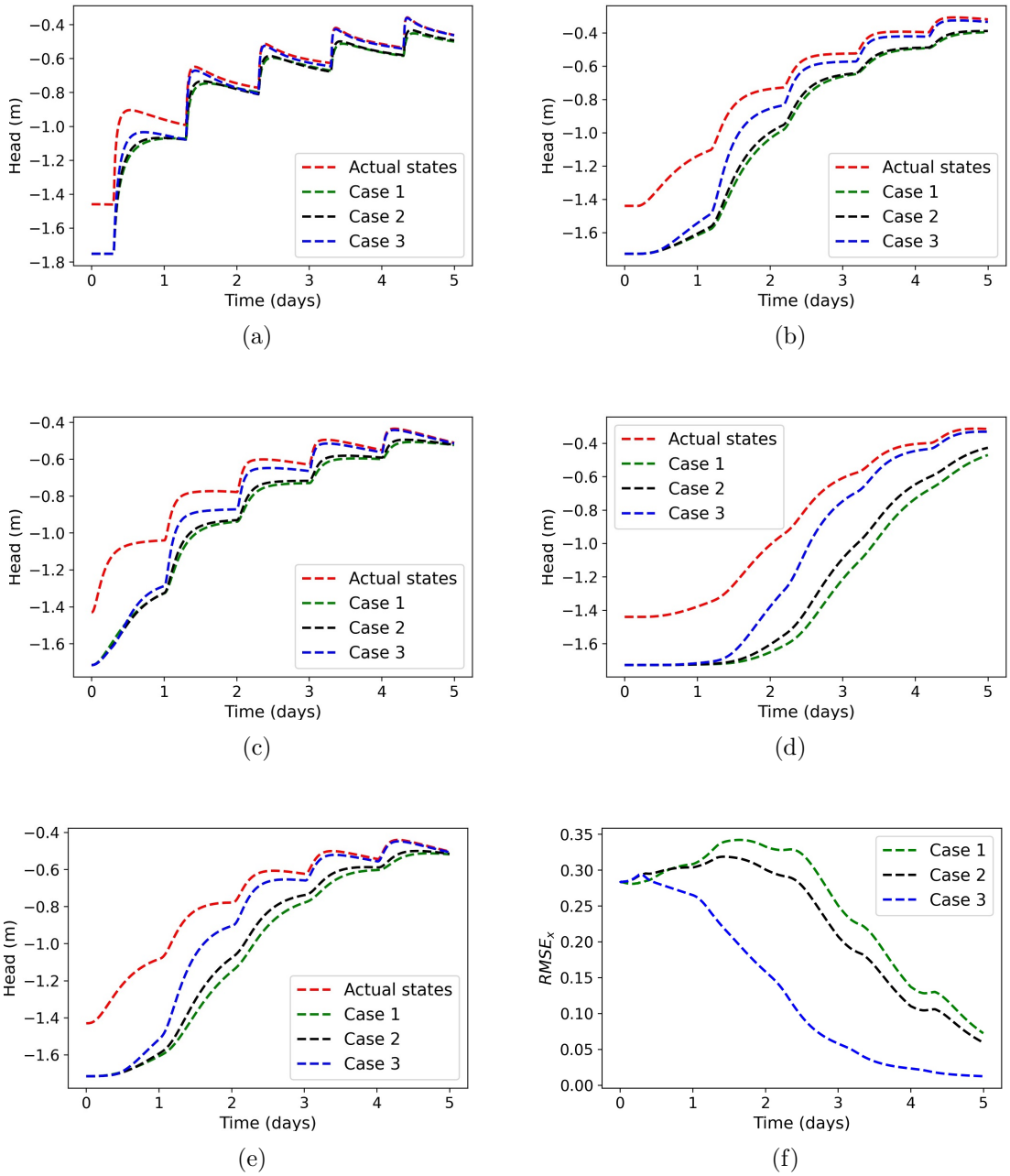

Figure 3.9: (a)-(e) Trajectories of the actual states (red lines), estimated states in Case 1 (green lines), estimated states in Case 2 (black lines), and estimated states in Case 3 (blue lines). (f) Evolution of the RMSE of the original state vector during the simulation time in Case 1 (red lines), Case 2 (blue lines) and Case 3 (black lines).

Table 3.3 shows the average performance indexes for the entire simulation of the three cases in the second scenario. From Table 3.3, it can be observed that the average RMSE of the state vector, parameter vector and entire augmented state vector in case 3 are smaller

than case 1 and case 2, which demonstrates the estimation performance in the proposed method is significantly improved.

Table 3.3: The average performance indexes for the entire simulation in scenario 2.

	$RMSE_x$	$RMSE_p$	$RMSE_{x_a}$
Case 1	26.29%		
Case 2	24.19%	14.20%	24.00%
Case 3	16.60%	13.90%	16.44%

3.4 Summary

In this work, a systematic procedure for simultaneous estimation of soil moisture and soil hydraulic parameters in 3D agro-hydrological systems with heterogeneous soils was proposed. Sensitivity analysis and orthogonalization were used to explore the degree of observability of hydraulic parameters every sampling time. Two different simulation case studies were carried out to illustrate the procedure. It was demonstrated that a significant improvement in estimation performance could be achieved with the proposed approach.

Chapter 4

Surface Soil Moisture Remote Sensing Through Machine Learning

Point soil moisture sensors used in the previous chapters provide soil moisture measurements for sparse point locations. It is impractical to install point sensors everywhere in the field for obtaining a thorough water distribution. Remote sensing provides an affordable and feasible way to obtain soil moisture measurements of the entire field. In this chapter, we propose to estimate surface soil moisture using thermal and optical remote sensing images and weather conditions as the inputs to the system through a machine learning-based Multilayer Perceptron (MLP). The MLP is a class of feedforward artificial neural networks (ANNs) that is widely used for supervised learning. First, the collection procedure of remote sensing images and soil moisture data from the 2019 demo farm experiment is discussed. The details of different vegetation indexes and model development are then discussed. Next the surface soil moisture estimation method using the remote sensing images is proposed. There is a detailed description of how the real data set is created from the experimental remote sensing images collected in summer 2019 at Lethbridge. In the end, the MLP model is trained using the real data set to provide surface soil moisture. Soil moisture estimation results are analyzed to investigate the efficacy of the proposed model.

4.1 Remote Sensing and Soil Moisture Data Collection Procedure

This section discusses the last experiment conducted on the actual agricultural field described in Section 2.1 in summer 2019. In this experiment, the thermal and optical remote sensing images were obtained by flying a drone, and at the same time, the soil moisture at a few specific locations on the surface of the field was collected using point soil moisture sensors. In the rest of this chapter, firstly the collection procedure of remote sensing images from the drone is discussed and the soil moisture data collection procedure is then explained. The detailed information on the experiment is provided in [3].

4.1.1 Remote Sensing Image Collection Using Drone

During the experiment, the RGB and thermal images were captured with the DJI Mavic 2 Enterprise Dual [59], and the NIR images and the blue NDVI values were obtained with the AgroCam NDVI camera [60]. In addition to the thermal camera which was already integrated with the drone, the Agrocam NDVI camera was also attached to the drone using the GPS and integration modules. As a result, all three spectral (RGB, NIR, and thermal) images were obtained simultaneously. The drone and the Agrocam are shown in Figure 4.1 from [59, 60].

(a) (b)

Figure 4.1: a) DJI Mavic 2 Enterprise Dual, (b) AgroCam.

There are some important flight details such as: 1) flight altitude: 80 ft, 2) front and side overlap: 80% and 75%, and flight speed: 7 mph. It is notable to mention that the thermal camera used in this experiment does not provide radiometric thermal images and it only gives the cold and hot area for the particular image. This issue has been addressed in [3] by taking the video of the thermal images and converting the thermal images to radiometric thermal images. The details of conversion and the flight operation checklist are discussed in [3]. The captured remote sensing images are used in this chapter as the inputs to the machine learning-based model.

4.1.2 Soil Moisture Data Collection

To train and validate the machine learning-based model, soil moisture collection is required. In the experiment, hand-held sensors [61] were used to measure the surface soil moisture, soil temperature and electric conductivity. Figure 4.2 shows the hydrago sensor used in the experiment.

Figure 4.2: Steven hydrago sensor.

The surface soil moisture data were collected at specific locations in the field while the drone was flying and the remote sensing images were captured. The location of the hydrogo sensors is shown in Figure 2.1(b). The surface soil moisture from the hydrago sensors were collected from all the 20 locations. In the following, we summarize the procedure of data collection in this experiment. We first flew the drone between the time 8.00 AM to 10 AM daily to capture the RGB, thermal, and NIR images. During the flying of the drone, we collected the soil moisture at some specific locations on the surface of the field using steven probe sensors. At the same time, the weather data was also recorded from the weather information website.

4.1.3 Data Pre-processing

The remote sensing images collected from the drone and the soil moisture sensors obtained from probe sensors are required to be pre-processed before using in the soil moisture estimation. Sahoo [3] performed some pre-processing steps to address the issues existing in the collected data and prepare them for estimation. Converting thermal images to radiometric thermal images to provide accurate temperature information, image registration and stitching to form a completed map of the field, and identifying the sensor locations on the image are the main pre-processing steps that were performed on the data by Sahoo [3].

In this thesis, we use the pre-processed images and data obtained from [3]. The remote sensing images and soil moisture data are available from July 2^{nd}, 2019 to July 31^{st}, 2019 on the date {2,4,9,11,15,17,19,22,23,26,29,30,31}. On each day, there are three maps of the entire field: 1) RED map; 2) NIR map; 3) Thermal map. Note that from RGB images, red, green, and blue maps can be obtained. But in this work, we focus on using only RED maps. Based on the maps, RED, NIR, and temperature values of the entire field surface can be obtained. In addition, the soil moisture data for all 20 locations on the surface of the field is available for each day. As an example, Figure 4.3 and Table 4.1 respectively represent the remote sensing maps and soil moisture data on 4^{th} July, 2019.

(a) RED map

(b) NIR map

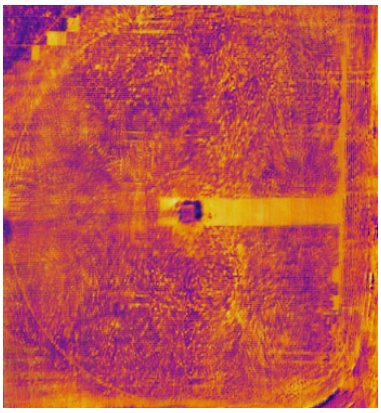

(c) Thermal map

Figure 4.3: Remote sensing maps of the entire field on 4^{th} July, 2019.

Table 4.1: Soil moisture measurements from probe sensors on 4^{th} July, 2019.

Sensor position	Point 1	Point 2	Point 3	Point 4	···	···	Point 20
Soil moisture	0.17	0.21	0.18	0.19	···	···	0.18

4.2 Methods

In this section, we discuss the different input indexes and model development for the soil moisture estimation.

4.2.1 Normalized Difference Vegetation Index (NDVI)

Normalized Difference Vegetation Index (NDVI) is a commonly provided index that measures crop health and photosynthetic activity. The higher the index value the greater the crop vigor. The NDVI is determined by measuring how much light the plant reflects at specific frequencies. In healthy plants, the leaves strongly reflect near-infrared light and strongly absorb red light. Whereas, dehydrated and unhealthy plants lose their spongy layers, which causes the leaves to absorb more near-infrared light. Thus, NDVI can be calculated as follows:

$$NDVI = \frac{NIR - RED}{NIR + RED} \tag{4.1}$$

where NIR is the near-infrared reflectivity and RED is the red reflectivity. NDVI values range from -1 to 1; numbers between -1 and 0 represent dead plants or inanimate objects, 0 to 0.33 represent a stressed plant, 0.33 to 0.66 represent a moderately healthy plant, and 0.66 to 1 is a very healthy plant. For example, Figure 4.4 represents the near-infrared and RGB image of two plants, one is healthy and the other one is unhealthy [2]. From Figure 4.4, we can observe the healthy plant (left image) absorbs a lot of visible light and reflects a large portion of near-infrared light. Whereas, unhealthy or sparse vegetation (right image) absorbs more visible light and reflects less near-infrared light. Based on NDVI formulation, the NDVI value for healthy plant, $\frac{0.50-0.08}{0.50+0.08} = 0.72$, is much bigger than dead plant one $\frac{0.40-0.30}{0.40+0.30} = 0.14$.

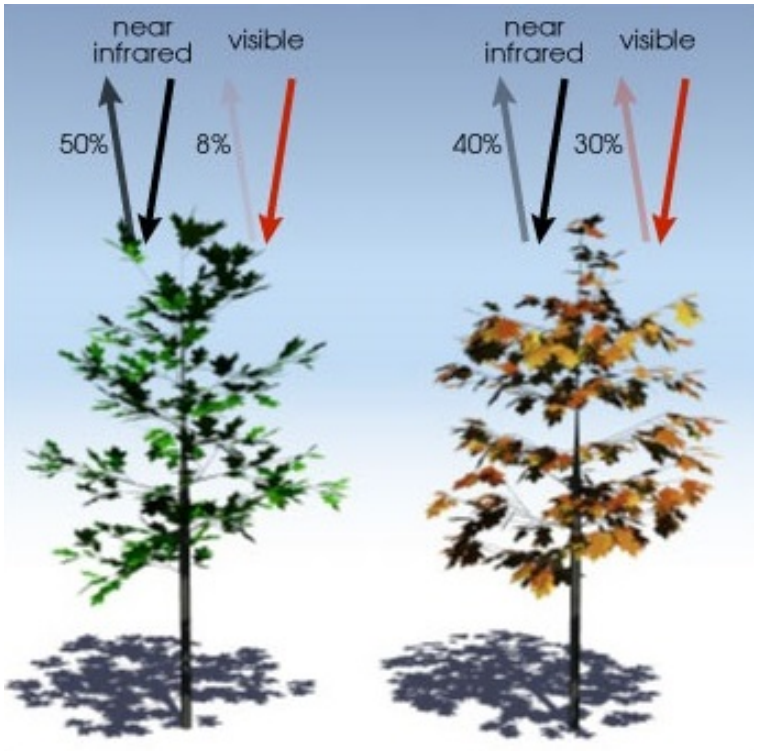

Figure 4.4: NDVI analysis of healthy and unhealthy plant from [2]

4.2.2 Temperature Vegetation Dryness Index (TVDI)

Surface temperature and vegetation index (NDVI) are combined to create the Temperature Vegetation Dryness Index (TVDI). The TVDI is calculated using the following equation [39]:

$$TDVI = \frac{T_s - T_{s,min}}{T_{s,max} - T_{s,min}} \tag{4.2}$$

where T_s is the observed land surface temperature at the given pixel; $T_{s,min}$ is the lowest surface temperature given the NDVI along the wet edge; $T_{s,max}$ is the maximum surface temperature given the NDVI along the dry edge which can be expressed as a function of NDVI ($T_{s,max} = a+b\,(NDVI)$), a, b are the coefficients of the dry edge. Figure 4.5 represents the T_s and $NDVI$ feature space which is plotted as a triangular area. Wet edge can be viewed as a constant bottom line of the triangle, whereas the dry edge is represented as the diagonal line of the triangle which varies linearly with the NDVI. The ET shows the evapo-transpiration term. For full cover plant, the ET is maximum and for bare soil the ET is minimum. More details of the TVDI methods can be found in [39].

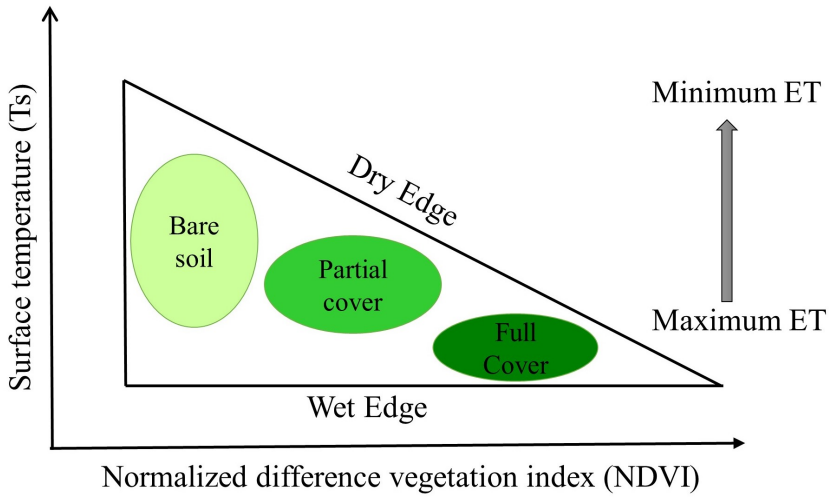

Figure 4.5: T_s-NDVI triangle feature space [3].

4.2.3 Multilayer Perceptron (MLP) Modeling

In this section, we give a brief overview of multilayer perceptron artificial neural networks. Multilayer perceptron (MLP) is a class of feedforward artificial neural networks (ANNs). MLPs are designed to approximate any continuous function and can solve problems which are not linearly separable. The major use cases of MLP are pattern classification, recognition, prediction and approximation. MLP is based on the supervised procedure which means the network builds a model based on examples in data with known outputs [62, 63]. The architecture of the MLP is completely defined by an input layer, one or more hidden layers, and an output layer. Each layer consists of at least one neuron called perceptron. Figure 4.6 illustrates the configuration of the MLP, from [4]. The input layer receives the input signal to be processed. The required task such as prediction and classification is performed by the output layer. An arbitrary number of hidden layers that are placed in between the input and output layer are the true computational engine of the MLP. In the MLP, the data flows in the forward direction from input to output layer.

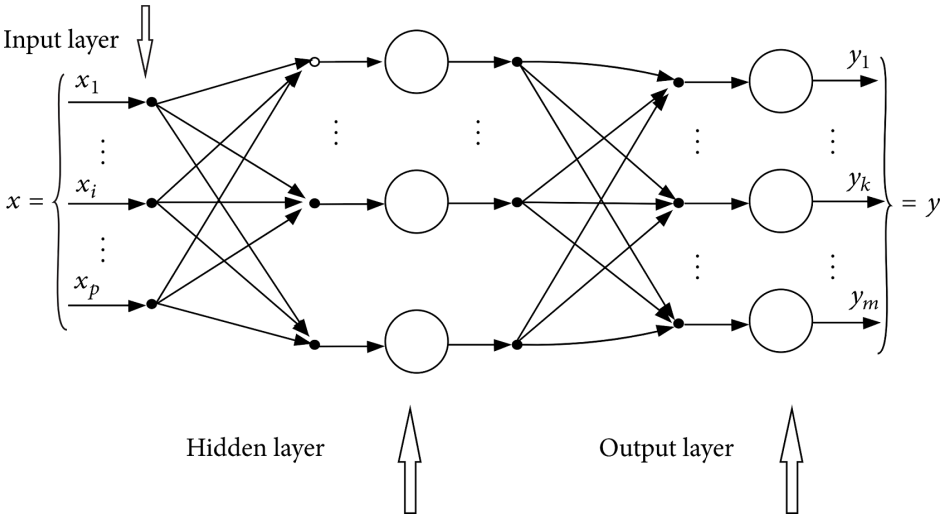

Figure 4.6: General architecture of multilayer perceptron neural network model [4]

The perceptrons in the MLP are trained with the backpropagation learning algorithm. The backpropagation algorithm is summarised below [64, 65].

1. Initialise network weights

2. Present first input vector, from training data, to the network

3. Propagate the input vector through the network to obtain an output

4. Calculate an error signal by comparing actual output to the desired (target) output

5. Propagate error signal back through the network

6. Adjust weights to minimise overall error

7. Repeat steps 2-7 with next input vector, until overall error is satisfactorily small

In the following, we describe how a perceptron uses the given inputs to calculate the corresponding output, i.e., how forwarding propagation (step 3) is accomplished in the above algorithm. Figure 4.7 shows a general appearance of a neuron with its connections [5]. Each connection from ith to the jth neuron is associated with a quantity called weight or connection strength (wij).

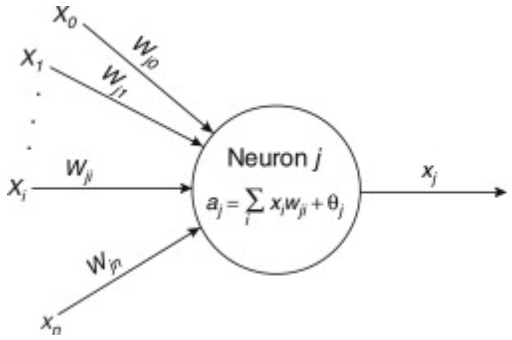

Figure 4.7: Basic processing element (perceptron) in a network. Each input connection value (x_i) is associated with a weight (W_{ji}). The output value ($x_j = f(a_j)$) can fan out to another unit [5]

A net input (called activation) for each neuron is the sum of all its input values multiplied by their corresponding connection weights, expressed as [66]

$$a_j = \sum_{i=1}^{n} x_i w_{ji} + \theta_j \tag{4.3}$$

where i is the total of neurons in the previous layer and θ_j is a bias term which influences the horizontal offset of the function. Once the activation of a perceptron is calculated, the result of this computation is then passed onto a nonlinear activation function f, which will produce the output of the perceptron [5]:

$$x_j = f(a_j) \tag{4.4}$$

Many activation functions may be used, for example, a linear function, a threshold function, a sigmoid function, etc, as shown in Figure 4.8.

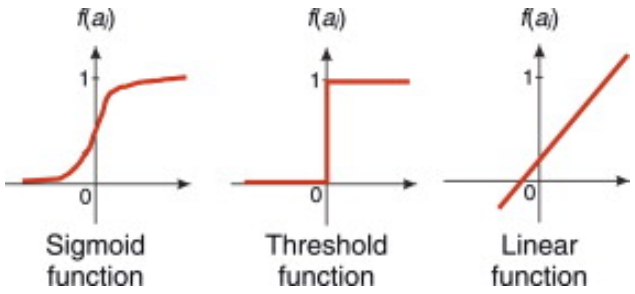

Figure 4.8: Three types of nonlinear activation functions commonly used in ANN models [5].

A sigmoid function is often used, because it has nonlinearity, which is given by:

$$x_j = f(a_j) = \frac{1}{1 + \exp(-a_j)} \tag{4.5}$$

The weights play an important role in the propagation of the signal in the network. They establish a link between input pattern and its associated output pattern, that is, they contain the knowledge of the neural network about the problem–solution relation. The forward-propagation step begins with the presentation of an input pattern to the input layer, and continues as activation-level calculations propagate forward till the output layer through the hidden layer(s). In each successive layer, every neuron sums its inputs and then applies a transfer function to compute its output. The output layer of the network then produces the final response, that is, the estimate of target value.

4.3 Proposed Soil Moisture Estimation Method

In this section, we propose a supervised estimation of surface soil moisture using a multilayer perceptron artificial neural network model. Initially, the MLP model is trained by using surface soil moisture probe measurements at a few sensor locations as the output of the model, and remote sensing images as the inputs. The trained MLP model can then be used to calculate the surface soil moisture of the entire field. Mathematically it can be written as follows:

$$y = f(u) \tag{4.6}$$

where y is the surface soil moisture. f is a nonlinear function that maps remote sensing images to the soil moisture. MLP neural network is used in this section to approximate that function. u represents the inputs to the system which consist of two main parts: 1) remote sensing images includes NDVI and TVDI images; 2) irrigation and climate data includes rain and evapo-transpiration (ET). Note that when we fly the drone, we usually do not obtain remote sensing images every day, whereas climate data can be obtained every day. Thus in the proposed method, we consider irrigation and climate data for some specific days that the remote sensing images are available. Figure 4.9 shows the proposed method for entire farm's soil moisture estimation from the remote sensing images. In the following we explain how the MLP model is trained in the proposed method.

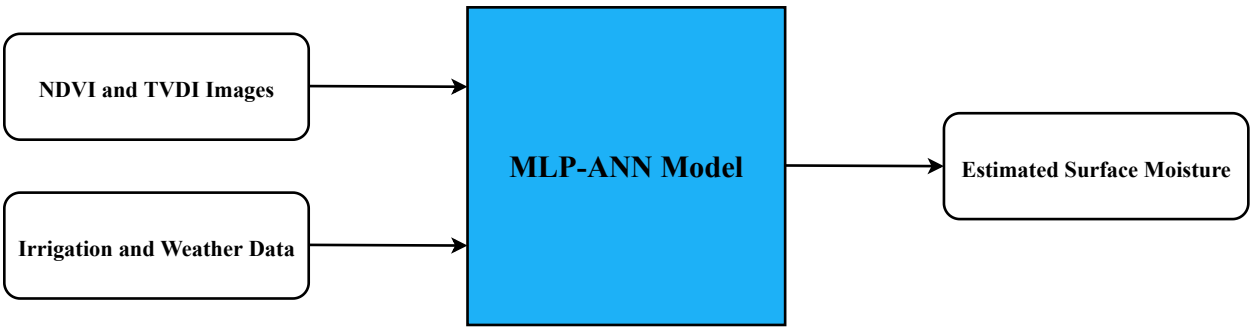

Figure 4.9: Flow diagram of proposed soil moisture estimation

According to Section 4.1.3, the remote sensing images and soil moisture data are available from July 2^{nd}, 2019 to July 31^{st}, 2019 on the dates {2,4,9,11,15,17,19,22,23,26,29,30,31}. On each day, there are RED, NIR, and thermal maps of the entire field and soil moisture of 20 locations on the surface. The following is a step-by-step description of how the real data set is derived from the experimental images conducted in the summer of 2019 at Lethbridge and how the MLP model is trained using the resulting data set.

1. Choose the first date of data: July 2^{nd}.

2. Collect RED, NIR, and thermal maps of the entire field as well as soil moisture data at 20 sensor locations for the selected date. For example, Figure 4.10 and Table 4.2 respectively represent the remote sensing maps and soil moisture data on 2^{nd} July, 2019.

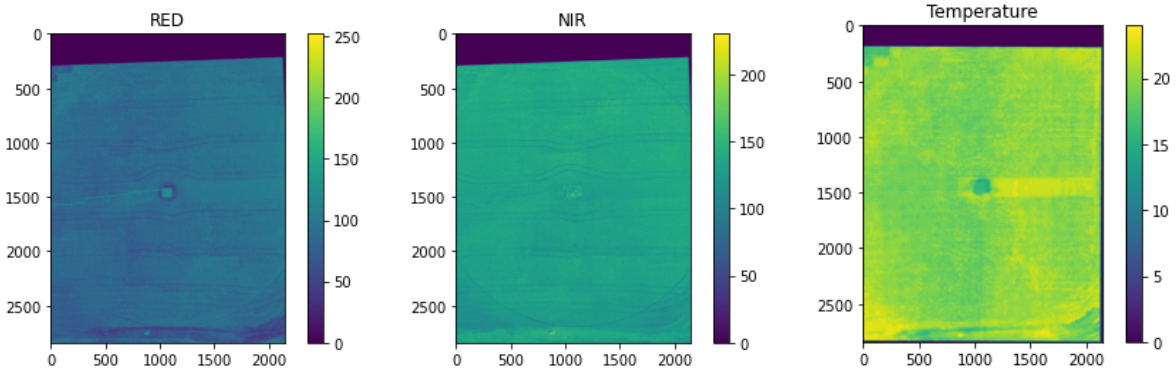

(a) RED map (b) NIR map (c) Thermal map

Figure 4.10: Remote sensing maps of the entire field on 2^{nd} July, 2019.

Table 4.2: Soil moisture measurements from probe sensors on 2^{nd} July, 2019.

Sensor position	Point 1	Point 2	Point 3	Point 4	⋯	⋯	Point 20
Soil moisture	0.19	0.22	0.17	0.18	⋯	⋯	0.17

3. Obtain climate data including rain and ET for the selected date from the weather station near the demo farm from website (https://agriculture.alberta.ca/acis/). Irri-

gation amount and scheduling of the demo farm can be also obtained from Table 2.1 in Section 2.6.

4. Use Equations (4.1,4.2) to respectively obtain NDVI and TVDI maps of the entire field for the selected date using RED, NIR, and thermal maps obtained from step 2. Figure 4.11 illustrates the TVDI and NDVI maps obtained on 2^{nd} July, 2019.

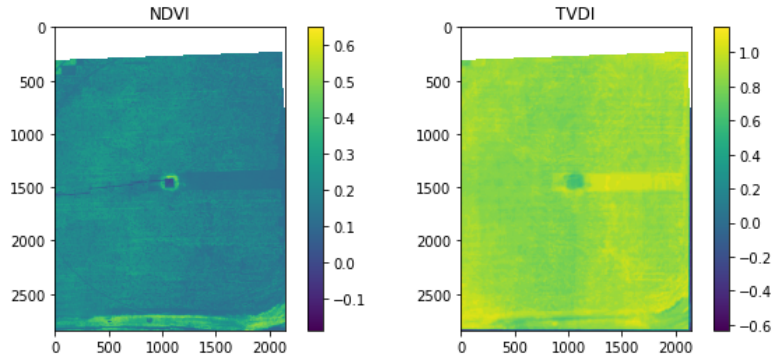

(a) NDVI map (b) TVDI map

Figure 4.11: NDVI and TVDI maps of the entire field on 2^{nd} July, 2019.

5. The sensor locations on the image have been identified using the minimum distance between GPS coordinates of the marked sensor locations and the pixels of the stitched image [3]. However, the image registration between different NIR, thermal and RGB images is not always perfect. Thus in the proposed method, in order to address the misregistration issue, we use the averaging method around the sensor location. We consider a small rectangle around the sensor pixels and average the values inside the rectangle. The average value will be used as an input to the MLP instead of only one selected sensor pixel value. Figure 4.12 shows the identified sensor locations and averaging rectangle on NIR image of 2^{nd} July, 2019. Hence at this step, we calculate the average NDVI and TVDI values inside the rectangle surrounding all 20 sensor pixels.

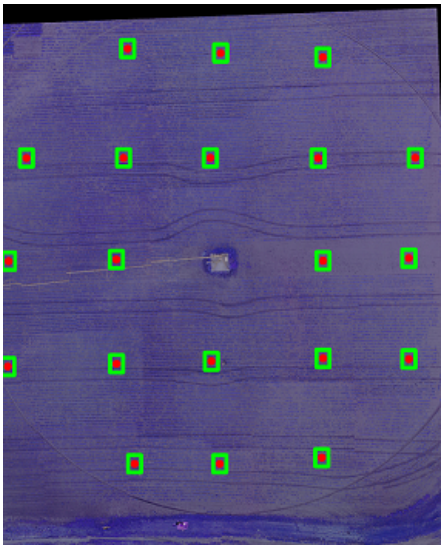

Figure 4.12: Identified sensor locations and rectangles around sensor pixels on NIR image of 2^{nd} July, 2019.

6. Place all the information obtained from steps 2 to 5 for the selected date together in the following table. Table 4.3 summarizes all collected information on 2^{nd} July, 2019. From Table 4.3, there are 20 samples in the first date.

Table 4.3: Collected information on 2^{nd} July, 2019.

Sample	NDVI(X_1)	TVDI(X_2)	Irrigation(X_3)	Rain(X_4)	ET(X_5)	Soil moisture(Y)
1	0.18	0.91	0	0	2.7	0.17
2	0.19	0.81	0	0	2.7	0.27
⋮	⋮	⋮	⋮	⋮	⋮	⋮
19	0.18	0.88	0	0	2.7	0.14
20	0.20	0.83	0	0	2.7	0.14

7. Go back to the first step and set the next date on which data is available and repeat steps 2 to 6. Add the collected information on the new date to the previous table. Repeat the same procedure for all 13 dates of July in which data are available in order to complete the table. Table 4.4 represents all information collected for all days. There are 20 samples for each date. For example, rows from 1 to 20 represent information collected on 2^{nd} July, or samples between 21 and 40 include information on 4^{th} July.

Table 4.4: Data set including inputs and output of the system.

Sample	NDVI(X_1)	TVDI(X_2)	Irrigation(X_3)	Rain(X_4)	ET(X_5)	Soil moisture(Y)
1	0.18	0.91	0	0	2.70	0.17
⋮	⋮	⋮	⋮	⋮	⋮	⋮
20	0.20	0.83	0	0	2.70	0.14
21	0.21	0.85	1.81	0.50	1.80	0.17
⋮	⋮	⋮	⋮	⋮	⋮	⋮
40	0.22	0.98	1.81	0.50	1.80	0.15
⋮	⋮	⋮	⋮	⋮	⋮	⋮
⋮	⋮	⋮	⋮	⋮	⋮	⋮
240	0.30	0.65	0	5.30	0	0.29
⋮	⋮	⋮	⋮	⋮	⋮	⋮
260	0.32	0.54	0	5.30	0	0.41

8. Table 4.4 is the data set used in the proposed method to train the MLP model. According to the obtaining data set, there are 260 samples, 5 main features, and 1 output. NDVI, TVDI, irrigation, rain, and ET are the 5 main features that are treated as the inputs to the MLP model. The soil moisture is also the only output of the MLP model. Note that, in the proposed method we consider only one MLP model for all days, and train it using the resulting data set which includes information about all days. Thus in the proposed method, a single MLP neural network is developed to predict the surface soil moisture on all days. Table 4.5 summarizes the description of data set used for the MLP neural network simulations.

Table 4.5: Data set statistics.

	NDVI	TVDI	Irrigation (mm)	Rain (mm)	ET (mm)	Soil moisture
Count	260	260	260	260	260	260
Mean	0.304	0.703	0.498	0.262	5.215	0.233
Standard deviation	0.086	0.152	0.752	0.602	1.568	0.089
Minimum	0.116	0.313	0	0	1.8	0.07
Maximum	0.478	1.102	1.81	2.2	8	0.44

9. Determine the neural network structure. Select the number of MLP neural network layers, the number of neurons in each layer, the optimizer, activation functions, the batch size, and epochs for model fit. Note that there are no universal rules for determining these parameters and they are usually chosen by trial-and-error experimentation.

10. Normalize the data set and split it into training and validation sets. The training data set is used to fit the MLP model and the validation data set is used to evaluate the performance of the trained MLP model.

4.4 Results

In this section, the proposed method and the real data set, is used to train a MLP neural network model. The main purpose of MLP model is to estimate the surface soil moisture of the entire field using remote sensing images. Data variables in Table 4.4 have different ranges of values and units. Thus before using the data set in the training process, data variables need to be standardized. The input data are normalized within the range of 0 and 1 using the following function:

$$X_{ij} = \frac{x_{ij} - V_{minj}}{V_{maxj} - V_{minj}} \tag{4.7}$$

where X_{ij} is the normalized value of the input x_{ij}, V_{minj} and V_{maxj} the minimum and maximum values of the j^{th} variable in all observations, respectively. The 260 samples are split into two sets: 208 samples are used to train the model and the other 52 samples for validation. The validation set which has not been seen in the model training is used to evaluate the performance of the trained model. To verify the effectiveness of the proposed method, two different regression models are considered: 1) Linear regression model; 2) MLP neural network regression model. The root mean squared error (RMSE) and the coefficient of determination (R^2) are used to assess the performance of the trained model in soil moisture estimation.

4.4.1 Linear Regression Model

In the first case, a linear regression model is used to describe the relationship between the soil moisture as the output of the system and remote sensing images and climate data as the inputs to the system. Mathematically the linear regression model in this work can be expressed as:

$$y = \theta_1 x_1 + \theta_2 x_2 + \theta_3 x_3 + \theta_4 x_4 + \theta_5 x_5 + \theta_6 \tag{4.8}$$

where y is the soil moisture, x_1 to x_5 are the five features of the system (NDVI, TVDI, Irrigation, Rain, and ET), and θ_1 to θ_6 are the parameters of the linear model that need to be estimated. The most common type of approach to train the linear regression equation from set of data is ordinary least squares (OLS) technique. OLS estimates the coefficients of linear model by minimizing the residual sum of squares between the observed targets in the data set, and the targets predicted by the linear approximation. In this work, the real data set obtained in Table 4.4 is used to fit the coefficients of linear model in Equation (4.8). Figure 4.13 shows the training and validation measurement points vs. the predicted points obtained from the fitted linear model at the same location in two different plots.

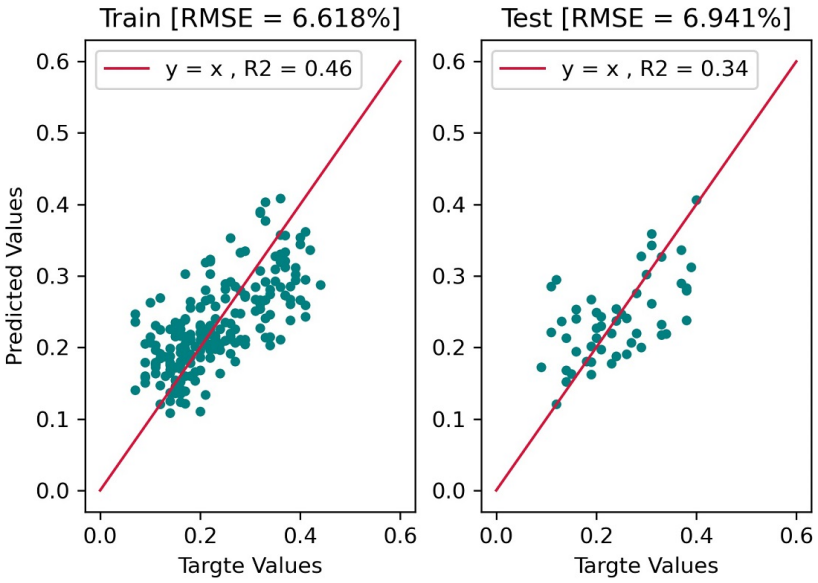

Figure 4.13: Measured and predicted soil moisture scatter plot in Linear regression.

Based on the results, RMSE for training points is 6.62% and for validation points is 6.94%. In addition, the R^2 for the validation points is 0.34 while for the training points is 0.46. For further analysis, the training and validation results of the predicted and measured soil moisture are shown respectively in Figures 4.14 and 4.15. We can see that the predicted values from the linear regression follow the trend of the measured soil moisture.

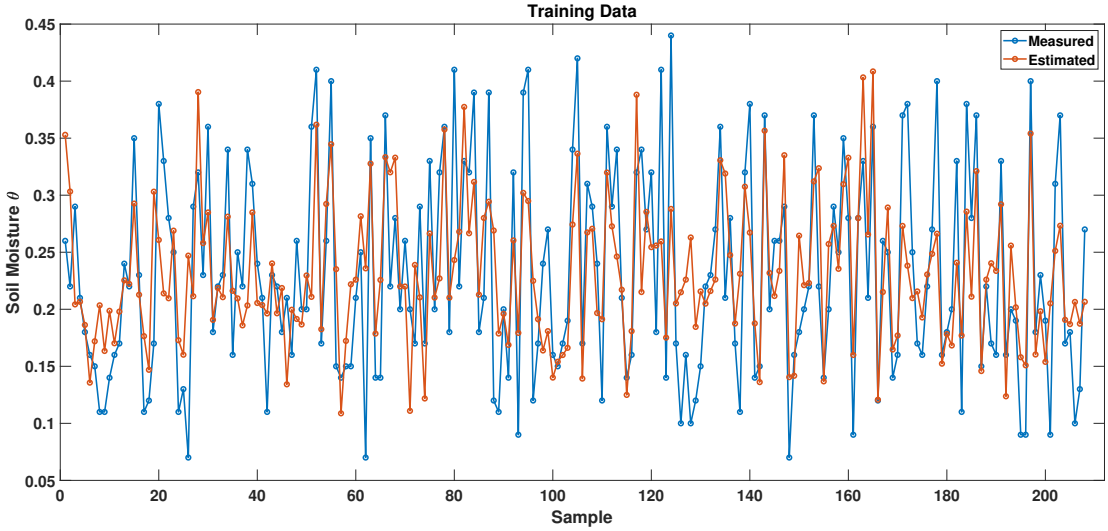

Figure 4.14: A comparison of the measured soil moisture (blue dots) with their corresponding estimates (red dots) for the training set in linear regression.

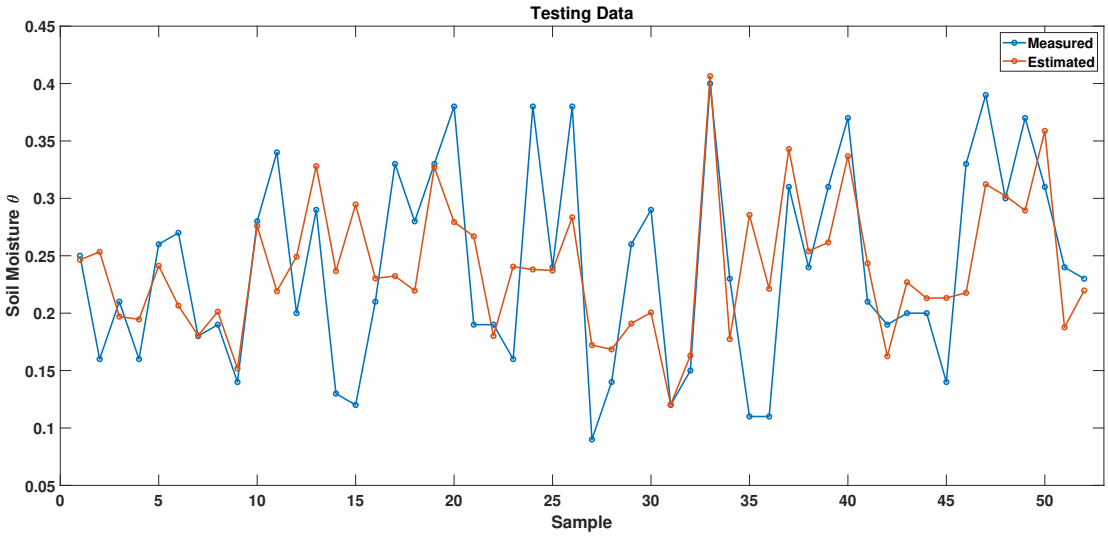

Figure 4.15: A comparison of the measured soil moisture (blue dots) with their corresponding estimates (red dots) for the validation set in linear regression.

4.4.2 MLP Regression Model

In the second case, a MLP neural network model is used to predict the surface soil moisture using the remote sensing images and climate data. In the structure of the MLP network, two hidden layers with 55 neurons are used. The maximum iteration and batch size are 300 and 4, respectively. The ReLU (Rectified Linear Unit) activation function for the hidden layers is used. In the process of training, the performance function is mean squared error (MSE) and the solver for weight optimization is adam (a stochastic gradient-based optimizer). The real data set obtained in Table 4.4 is used to train the described MLP.

Figure 4.16 shows the training and validation measurement points vs. the predicted points at the same location in two different plots. The results illustrate that most of the validation and training points are near the 45° line. RMSE for training points is 4.07% and for validation points is 4.56% that are much smaller than linear regression errors. In addition, the R^2 for the training points is 0.80 and for the validation points is 0.71 which shows the superiority of the proposed algorithm and MLP model.

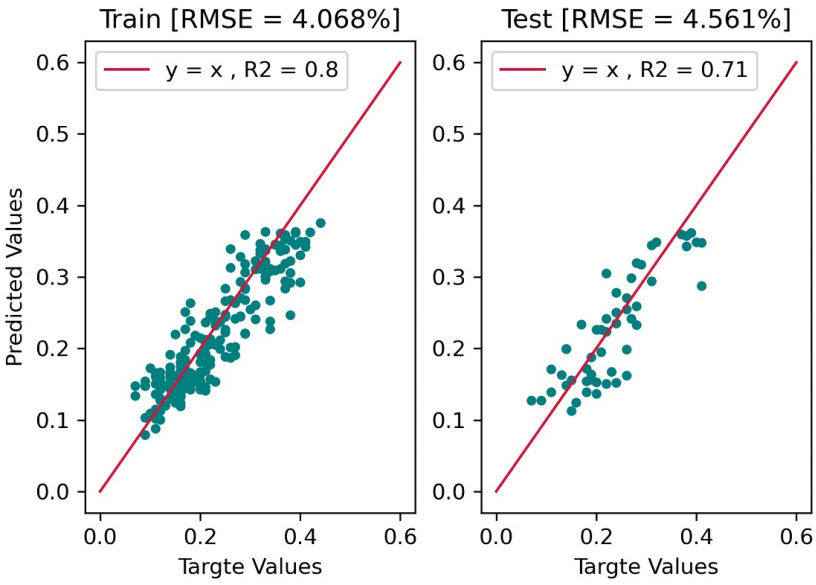

Figure 4.16: Measured and predicted soil moisture scatter plot in MLP neural network regression.

Figures 4.17 and 4.18 respectively represent the training and validation results of the predicted and measured soil moisture. We can observe that the predicted output from the MLP model has strong agreement with the measured soil moisture. Thus the performance of surface soil moisture estimation is significantly improved using the proposed method and MLP neural network model.

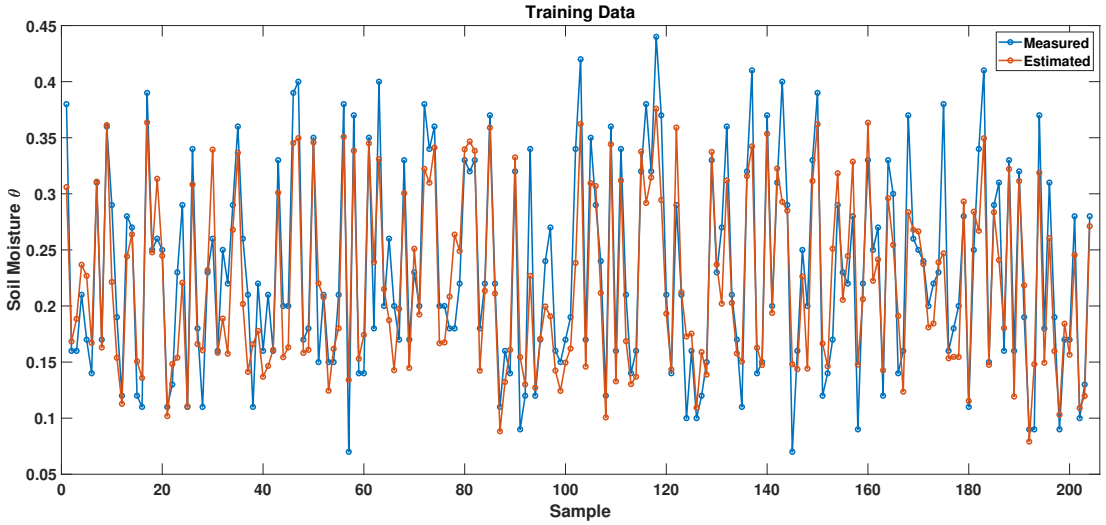

Figure 4.17: A comparison of the measured soil moisture (blue dots) with their corresponding estimates (red dots) for the training set in MLP neural network regression.

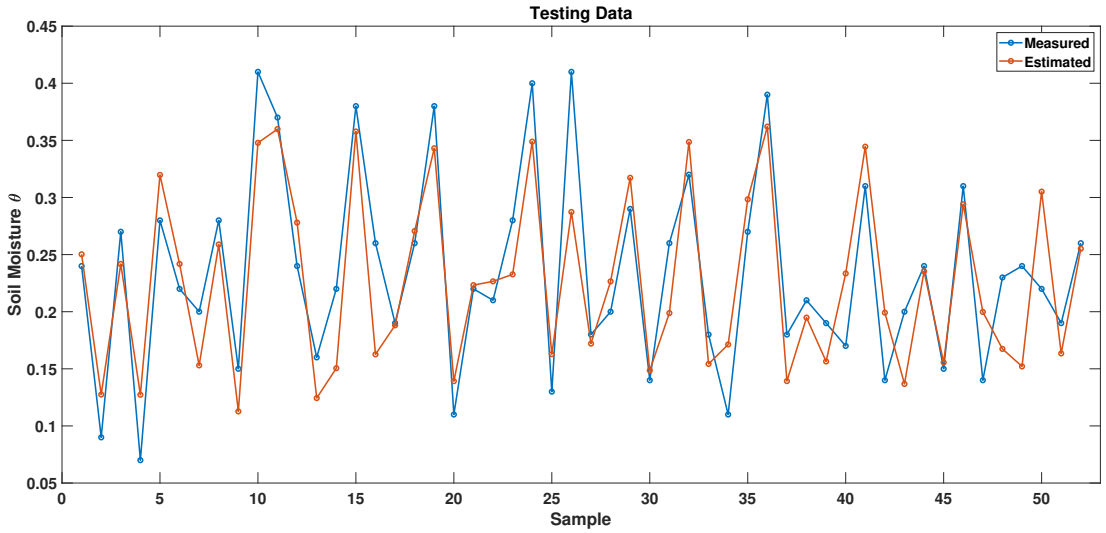

Figure 4.18: A comparison of the measured soil moisture (blue dots) with their corresponding estimates (red dots) for the validation set in MLP neural network regression.

4.5 Summary

In this chapter, we presented the algorithm to estimate the surface soil moisture from optical and thermal remote sensing images using the MLP neural network model. The surface soil moisture was estimated using the drone remote sensing images for a real field. The input to the MLP model was NDVI and TVDI images, rain, ET, and irrigation amount. The MLP was trained using the measured surface soil moisture collected from the hydroprobe sensors. The predicted output from the MLP model at both validation and training points showed a strong agreement with the measured soil moisture with R^2 0.71 and 0.80, respectively.

Chapter 5

Conclusions and Future Work

5.1 Conclusions

In this thesis, we addressed major challenges in soil moisture estimation for the application in large-scale agricultural fields. The impact of sensor placement in soil water estimation performance for an actual agricultural field and a simultaneous soil moisture and soil hydraulic parameter estimation of 3D field models were studied. Further, the remote sensing soil moisture estimation was discussed using the machine-learning based model.

In Chapter 2, an actual agriculture field was studied to investigate the impact of sensor placement in soil water estimation in an actual application. Initially, a description of the study area and the experiments carried out on the field was provided. A 3D agro-hydrological model was then developed using the cylindrical coordinate version of the Richards equation, in order to predict the soil moisture dynamics in the studied field and model the circular movement of the center pivot irrigation system. optimal sensor placement results were then obtained for the actual field by applying the modal degree of observability to the field model. It was found that in a field with 75 cm depth, measured states located at 65 cm below the surface layer, have relatively higher values of the modal degree of observability, while placing sensors on the surface gives the lowest modal degree of observability. The EKF algorithm

was then employed to estimate the soil water content of the studied field. According to the simulated case study results, the estimates converged faster to the actual states when the sensors were placed with a higher degree of observability. In addition, based on the simulation results, there was a significantly stronger agreement between the estimated moisture content maps and the actual moisture content maps in the case of optimal sensor placement. At the end of this chapter, the real measurements provided by watermark sensors were considered and two different scenarios were constructed: (i) in presence of two Measurements; (ii) in presence of a few measurements. In the real case study, two evaluation criteria were used to study the performance of the estimation. From the results of the performance evaluation, it was evident that the performance of state estimation with optimally sensor placement is significantly improved in the actual applications.

In Chapter 3, a systematic procedure was proposed to estimate the soil moisture and soil hydraulic parameters simultaneously for large-scale 3D agro-hydrological systems with heterogeneous soils and changing measurements. An agro-hydrological system equipped with a center pivot irrigation system and microwave soil moisture sensors was considered as the investigated system. By augmenting parameters at the end of the state vector and treating them as states, it was possible to estimate the states and parameters simultaneously. Based on the observability of the augmented system and the sensitivity of the outputs to the parameters, an algorithm was proposed for determining the appropriate parameter set for estimation. Next, the EKF estimation algorithm was chosen to simultaneously estimate the soil moisture and the set of soil hydraulic parameters which was earlier determined from the sensitivity analysis. In addition, in order to improve the performance of estimation, the Kriging interpolation method was employed for updating the unestimated parameters. The proposed method was then studied and evaluated with simulated measurements under the following scenario: (i) a small field with fixed measured states; (ii) a larger field with changing measured states. It was demonstrated that the proposed method could significantly improve the performance of soil moisture estimation and provide soil moisture estimates with high

accuracy and consistency under all the investigated scenarios.

In Chapter 4, MLP neural network model was proposed to estimate surface soil moisture using thermal and optical remote sensing images. The data which were collected from the experiment conducted in the summer of 2019 was used in this chapter. Initially, the definitions of various vegetation indices were explained. It was then explained in detail how the real data set was derived using experimental remote sensing images. The MLP was trained using the collected soil moisture. The estimated soil moisture from the MLP model at both training and validation points demonstrated a strong agreement with the measured soil moisture with R^2 0.8 and 0.71, respectively.

5.2 Future Work

- *State and parameter estimation using real measurements in an actual application* As a further step towards the simultaneous soil moisture and soil hydraulic parameter estimation, the proposed approach can be applied to a real agriculture field. In this thesis, it was found that the simultaneous state and parameter estimation based on the sensitivity analysis can improve the soil moisture estimation performance. However, it is unclear whether the significantly improved estimation performance can still be observed in the actual applications.

- *State and parameter estimation of completed agro-hydrological systems* In this thesis, the agro-hydrological system is modeled by Richards equation that only covers the water dynamics within soil. In the future work, evapo-transpiration model and crop growth model can be incorporated with Richards equation. The soil hydraulic parameter and soil moisture estimation problem can be studied on a completed agro-hydrological system.

Bibliography

[1] B. T. Agyeman, S. Bo, S. R. Sahoo, X. Yin, J. Liu, and S. L. Shah, "Soil moisture map construction by sequential data assimilation using an extended kalman filter," *Journal of Hydrology*, vol. 598, p. 126425, 2021.

[2] M. Ozyavuz, B. Bilgili, and A. Salici, "Determination of vegetation changes with ndvi method," *Journal of Environmental Protection and Ecology*, vol. 16, no. 1, pp. 264–273, 2015.

[3] S. R. Sahoo, *Model Reduction and Remote Sensing for Precision Irrigation Applications*. PhD thesis, University of Alberta, 2022.

[4] Z. Ali, I. Hussain, M. Faisal, H. M. Nazir, T. Hussain, M. Y. Shad, A. M. Shoukry, and S. H. Gani, "Forecasting drought using multilayer perceptron artificial neural network model," *Advances in Meteorology*, vol. 2017, 2017.

[5] S. Lek and Y. Park, "Multilayer perceptron," in *Encyclopedia of Ecology*, pp. 2455–2462, Oxford: Academic Press, 2008.

[6] "Waste water the untapped resource," *The United Nations World Water Development Report*, 2017.

[7] G. Fischer, F. N. Tubiello, H. V. Velthuizen, and D. A. Wiberg, "Climate change impacts on irrigation water requirements: Effects of mitigation, 1990–2080," *Technological Forecasting and Social Change*, vol. 74, no. 7, pp. 1083–1107, 2007.

[8] R. Romero, J. Muriel, I. García, and D. M. de la Peña, "Research on automatic irrigation control: State of the art and recent results," *Agricultural Water Management*, vol. 114, pp. 59–66, 2012.

[9] Y. Mao, S. Liu, J. Nahar, J. Liu, and F. Ding, "Soil moisture regulation of agro-hydrological systems using zone model predictive control," *Computers and Electronics in Agriculture*, vol. 154, pp. 239–247, 2018.

[10] J. Nahar, S. Liu, Y. Mao, J. Liu, and S. L. Shah, "Closed-loop scheduling and control for precision irrigation," *Industrial & Engineering Chemistry Research*, vol. 58, no. 26, pp. 11485–11497, 2019.

[11] S. R. Sahoo, X. Yin, and J. Liu, "Optimal sensor placement for agro-hydrological systems," *AIChE Journal*, vol. 65, no. 12, p. e16795, 2019.

[12] J. Nahar, J. Liu, and S. L. Shah, "Parameter and state estimation of an agro-hydrological system based on system observability analysis," *Computers & Chemical Engineering*, vol. 121, pp. 450–464, 2019.

[13] S. Bo, S. R. Sahoo, X. Yin, J. Liu, and S. L. Shah, "Parameter and state estimation of one-dimensional infiltration processes: A simultaneous approach," *Mathematics*, vol. 8, no. 1, p. 134, 2020.

[14] J. M. Sabater, L. Jarlan, J.-C. Calvet, F. Bouyssel, and P. De Rosnay, "From near-surface to root-zone soil moisture using different assimilation techniques," *Journal of Hydrometeorology*, vol. 8, no. 2, pp. 194–206, 2007.

[15] R. H. Reichle, J. P. Walker, R. D. Koster, and P. R. Houser, "Extended versus ensemble kalman filtering for land data assimilation," *Journal of Hydrometeorology*, vol. 3, no. 6, pp. 728–740, 2002.

[16] G. J. De Lannoy, R. H. Reichle, P. R. Houser, V. R. Pauwels, and N. E. Verhoest, "Correcting for forecast bias in soil moisture assimilation with the ensemble kalman filter," *Water Resources Research*, vol. 43, no. 9, 2007.

[17] H. Zhang, W. Kurtz, S. Kollet, H. Vereecken, and H.-J. H. Franssen, "Comparison of different assimilation methodologies of groundwater levels to improve predictions of root zone soil moisture with an integrated terrestrial system model," *Advances in Water Resources*, vol. 111, pp. 224–238, 2018.

[18] D. Pasetto, M. Camporese, and M. Putti, "Ensemble kalman filter versus particle filter for a physically-based coupled surface–subsurface model," *Advances in Water Resources*, vol. 47, pp. 1–13, 2012.

[19] H. Moradkhani, K.-L. Hsu, H. Gupta, and S. Sorooshian, "Uncertainty assessment of hydrologic model states and parameters: Sequential data assimilation using the particle filter," *Water Resources Research*, vol. 41, no. 5, 2005.

[20] J. P. Walker, G. R. Willgoose, and J. D. Kalma, "One-dimensional soil moisture profile retrieval by assimilation of near-surface measurements: A simplified soil moisture model and field application," *Journal of Hydrometeorology*, vol. 2, no. 4, pp. 356–373, 2001.

[21] J. Nahar, J. Liu, and S. L. Shah, "Observability analysis for soil moisture estimation," *IFAC-PapersOnLine*, vol. 50, no. 2, pp. 110–114, 2017.

[22] H. Lü, Z. Yu, Y. Zhu, S. Drake, Z. Hao, and E. A. Sudicky, "Dual state-parameter estimation of root zone soil moisture by optimal parameter estimation and extended kalman filter data assimilation," *Advances in Water Resources*, vol. 34, no. 3, pp. 395–406, 2011.

[23] H. Medina, N. Romano, and G. Chirico, "Kalman filters for assimilating near-surface observations into the richards equation–part 2: A dual filter approach for simultaneous

retrieval of states and parameters," *Hydrology and Earth System Sciences*, vol. 18, no. 7, pp. 2521–2541, 2014.

[24] H. Moradkhani, S. Sorooshian, H. V. Gupta, and P. R. Houser, "Dual state–parameter estimation of hydrological models using ensemble kalman filter," *Advances in Water Resources*, vol. 28, no. 2, pp. 135–147, 2005.

[25] W. Chen, C. Huang, H. Shen, and X. Li, "Comparison of ensemble-based state and parameter estimation methods for soil moisture data assimilation," *Advances in Water Resources*, vol. 86, pp. 425–438, 2015.

[26] C. Li and L. Ren, "Estimation of unsaturated soil hydraulic parameters using the ensemble kalman filter," *Vadose Zone Journal*, vol. 10, no. 4, pp. 1205–1227, 2011.

[27] C. Montzka, H. Moradkhani, L. Weihermüller, H.-J. H. Franssen, M. Canty, and H. Vereecken, "Hydraulic parameter estimation by remotely-sensed top soil moisture observations with the particle filter," *Journal of Hydrology*, vol. 399, no. 3-4, pp. 410–421, 2011.

[28] J. Liu, A. Gnanasekar, Y. Zhang, S. Bo, J. Liu, J. Hu, and T. Zou, "Simultaneous state and parameter estimation: the role of sensitivity analysis," *Industrial & Engineering Chemistry Research*, vol. 60, no. 7, pp. 2971–2982, 2021.

[29] G. P. Petropoulos, G. Ireland, and B. Barrett, "Surface soil moisture retrievals from remote sensing: Current status, products & future trends," *Physics and Chemistry of the Earth, Parts A/B/C*, vol. 83, pp. 36–56, 2015.

[30] M. Gupta, P. K. Srivastava, and T. Islam, "Integrative use of near-surface satellite soil moisture and precipitation for estimation of improved irrigation scheduling parameters," in *Satellite Soil Moisture Retrieval*, pp. 271–288, Elsevier, 2016.

[31] Y. Shi, K. J. Davis, F. Zhang, C. J. Duffy, and X. Yu, "Parameter estimation of a physically-based land surface hydrologic model using an ensemble Kalman filter: A multivariate real-data experiment," *Advances in Water Resources*, vol. 83, pp. 421–427, 2015.

[32] A. Ångström, "The albedo of various surfaces of ground," *Geografiska Annaler*, vol. 7, no. 4, pp. 323–342, 1925.

[33] L. Weidong, F. Baret, G. Xingfa, T. Qingxi, Z. Lanfen, and Z. Bing, "Relating soil surface moisture to reflectance," *Remote Sensing of Environment*, vol. 81, pp. 238–246, Aug. 2002.

[34] D. B. Lobell and G. P. Asner, "Moisture effects on soil reflectance," *Soil Science Society of America Journal*, vol. 66, no. 3, pp. 722–727, 2002.

[35] W. Liu, F. Baret, X. Gu, B. Zhang, Q. Tong, and L. Zheng, "Evaluation of methods for soil surface moisture estimation from reflectance data," *International Journal of Remote Sensing*, vol. 24, pp. 2069–2083, Jan. 2003.

[36] M. L. Whiting, L. Li, and S. L. Ustin, "Predicting water content using gaussian model on soil spectra," *Remote Sensing of Environment*, vol. 89, no. 4, pp. 535–552, 2004.

[37] D. Zhang and G. Zhou, "Estimation of soil moisture from optical and thermal remote sensing: A review," *Sensors*, vol. 16, no. 8, p. 1308, 2016.

[38] J. Peng, Y. Liu, and A. Loew, "Uncertainties in estimating normalized difference temperature index from toa radiances," *IEEE Transactions on Geoscience and Remote Sensing*, vol. 51, no. 5, pp. 2487–2497, 2012.

[39] I. Sandholt, K. Rasmussen, and J. Andersen, "A simple interpretation of the surface temperature/vegetation index space for assessment of surface moisture status," *Remote Sensing of Environment*, vol. 79, no. 2-3, pp. 213–224, 2002.

[40] Y. Han, Y. Wang, and Y. Zhao, "Estimating soil moisture conditions of the greater changbai mountains by land surface temperature and ndvi," *IEEE Transactions on Geoscience and Remote Sensing*, vol. 48, no. 6, pp. 2509–2515, 2010.

[41] J. Chen, C. Wang, H. Jiang, L. Mao, and Z. Yu, "Estimating soil moisture using Temperature–Vegetation Dryness Index (TVDI) in the Huang-huai-hai (HHH) plain," *International Journal of Remote Sensing*, vol. 32, pp. 1165–1177, Feb. 2011.

[42] T. Carlson, "An overview of the triangle method for estimating surface evapotranspiration and soil moisture from satellite imagery," *Sensors*, vol. 7, no. 8, pp. 1612–1629, 2007.

[43] D. Zhang, R. Tang, B.-H. Tang, H. Wu, and Z.-L. Li, "A simple method for soil moisture determination from lst–vi feature space using nonlinear interpolation based on thermal infrared remotely sensed data," *IEEE Journal of Selected Topics in Applied Earth Observations and Remote Sensing*, vol. 8, no. 2, pp. 638–648, 2014.

[44] M. E. Holzman, R. Rivas, and M. C. Piccolo, "Estimating soil moisture and the relationship with crop yield using surface temperature and vegetation index," *International Journal of Applied Earth Observation and Geoinformation*, vol. 28, pp. 181–192, 2014.

[45] D. Zhang, R. Tang, W. Zhao, B. Tang, H. Wu, K. Shao, and Z.-L. Li, "Surface Soil Water Content Estimation from Thermal Remote Sensing based on the Temporal Variation of Land Surface Temperature," *Remote Sensing*, vol. 6, pp. 3170–3187, Apr. 2014.

[46] P. Rahimzadeh-Bajgiran, A. A. Berg, C. Champagne, and K. Omasa, "Estimation of soil moisture using optical/thermal infrared remote sensing in the canadian prairies," *ISPRS Journal of Photogrammetry and Remote Sensing*, vol. 83, pp. 94–103, 2013.

[47] Z. Liu, Z. Yao, and R. Wang, "Evaluating the surface temperature and vegetation index (ts/vi) method for estimating surface soil moisture in heterogeneous regions," *Hydrology Research*, vol. 49, no. 3, pp. 689–699, 2018.

[48] L. Hassan-Esfahani, A. Torres-Rua, A. Jensen, and M. McKee, "Assessment of surface soil moisture using high-resolution multi-spectral imagery and artificial neural networks," *Remote Sensing*, vol. 7, no. 3, pp. 2627–2646, 2015.

[49] "Watermark sensors." `https://www.campbellsci.ca/253-l`.

[50] L. A. Richards, "Capillary conduction of liquids through porous mediums," *Physics*, vol. 1, no. 5, pp. 318–333, 1931.

[51] M. T. Van Genuchten, "A closed-form equation for predicting the hydraulic conductivity of unsaturated soils," *Soil Science Society of America Journal*, vol. 44, no. 5, pp. 892–898, 1980.

[52] F. Larguence, "Estimating soil contamination with kriging interpolation method," *American Journal of Applied Sciences*, vol. 3, pp. 1894–1898, 2006.

[53] M. A. Oliver and R. Webster, "Kriging: a method of interpolation for geographical information systems," *International Journal of Geographical Information System*, vol. 4, no. 3, pp. 313–332, 1990.

[54] R. F. Carsel and R. S. Parrish, "Developing joint probability distributions of soil water retention characteristics," *Water Resources Research*, vol. 24, no. 5, pp. 755–769, 1988.

[55] S. Gu, F. Pasqualetti, M. Cieslak, Q. K. Telesford, A. B. Yu, A. E. Kahn, J. D. Medaglia, J. M. Vettel, M. B. Miller, S. T. Grafton, *et al.*, "Controllability of structural brain networks," *Nature Communications*, vol. 6, no. 1, pp. 1–10, 2015.

[56] S. R. Sahoo, X. Yin, J. Liu, and S. L. Shah, "Dynamic model reduction and optimal sensor placement for agro-hydrological systems," *IFAC-PapersOnLine*, vol. 53, no. 2, pp. 11669–11674, 2020.

[57] "Casadi." `https://web.casadi.org`.

[58] J. Stigter, D. Joubert, and J. Molenaar, "Observability of complex systems: Finding the gap," *Scientific Reports*, vol. 7, no. 1, pp. 1–9, 2017.

[59] "Dji mavic 2 enterprise dual." `https://www.dji.com/ca/`.

[60] "Agrocam." `https://www.agrocam.eu`.

[61] "Hydrago sensors." `https://stevenswater.com/products/hydrago-s/`.

[62] A. Meyer-Baese and V. Schmid, "Chapter 7 - foundations of neural networks," in *Pattern Recognition and Signal Analysis in Medical Imaging (Second Edition)* (A. Meyer-Baese and V. Schmid, eds.), pp. 197–243, Oxford: Academic Press, second edition ed., 2014.

[63] S. Abirami and P. Chitra, "Energy-efficient edge based real-time healthcare support system," in *Advances in Computers*, vol. 117, pp. 339–368, Elsevier, 2020.

[64] M. Gardner and S. Dorling, "Artificial neural networks (the multilayer perceptron)—a review of applications in the atmospheric sciences," *Atmospheric Environment*, vol. 32, no. 14, pp. 2627–2636, 1998.

[65] C. M. Bishop, *Neural networks for pattern recognition*. Oxford University Press, 1995.

[66] T. Menzies, E. Kocagüneli, L. Minku, F. Peters, and B. Turhan, "Chapter 24 - using goals in model-based reasoning," in *Sharing Data and Models in Software Engineering*, pp. 321–353, Boston: Morgan Kaufmann, 2015.